

Joint modeling of low and high extremes using a multivariate extended generalized Pareto distribution

Noura Alotaibi^{a,b}, Matthew Sainsbury-Dale^a, Philippe Naveau^c, Carlo Gaetan^d, Raphaël Huser^{a,*}

^a*Statistics Program, CEMSE Division, King Abdullah University of Science and Technology (KAUST), Thuwal 23955–6900, Saudi Arabia*

^b*Department of Mathematics, College of Science, Imam Abdulrahman Bin Faisal University, Dammam 31113, Saudi Arabia*

^c*Laboratoire des Sciences du Climat et de l'Environnement, Bat 714 – ICE, 91191 Gif-sur-Yvette, France*

^d*Department of Environmental Sciences, Informatics and Statistics, Ca' Foscari University of Venice, 30123 Venice, Italy*

Abstract

In most risk assessment studies, it is important to accurately capture the entire distribution of the multivariate random vector of interest from low to high values. For example, in climate sciences, low precipitation events may lead to droughts, while heavy rainfall may generate large floods, and both of these extreme scenarios can have major impacts on the safety of people and infrastructure, as well as agricultural or other economic sectors. In the univariate case, the extended generalized Pareto distribution (eGPD) was specifically developed to accurately model low, moderate, and high precipitation intensities, while bypassing the threshold selection procedure usually conducted in extreme-value analyses. In this work, we extend this approach to the multivariate case. The proposed multivariate eGPD has the following appealing properties: (1) its marginal distributions behave like univariate eGPDs; (2) its lower and upper joint tails comply with multivariate extreme-value theory, with key parameters separately controlling dependence in each joint tail; and (3) the model allows for fast simulation and is thus amenable to simulation-based inference. We propose estimating model parameters by leveraging modern neural approaches, where a neural network, once trained, can provide point estimates, credible intervals, or full posterior approximations in

*Corresponding author.

Email addresses: `noura.alotaibi@kaust.edu.sa` (Noura Alotaibi), `matthew.sainsburydale@kaust.edu.sa` (Matthew Sainsbury-Dale), `philippe.naveau@lsce.ipsl.fr` (Philippe Naveau), `gaetan@unive.it` (Carlo Gaetan), `raphael.huser@kaust.edu.sa` (Raphaël Huser)

a fraction of a second. Our new methodology is illustrated by application to daily rainfall times series data from the Netherlands. The proposed model is shown to provide satisfactory marginal and dependence fits from low to high quantiles.

Keywords: Extreme-value theory, Likelihood-free inference, Lower and upper tails, Multivariate extremes, Neural Bayes estimation, Normalizing flows, Regular variation

1. Introduction

Record-breaking extreme weather events stemming from opposite distributional tails, such as heat and cold waves or floods and droughts, can both lead to major impacts and pose serious health, social, environmental, and economic risks (IPCC, 2023; Fischer et al., 2025). Widespread flooding, for example, affects people worldwide (Brunner et al., 2020) and is one of the costliest hazards in the United States according to Swiss Re (2019). Among other geo-environmental factors, flooding often results from excess precipitation, which can either be caused by a single heavy rainfall event or by several consecutive but potentially less extreme rainfall events, whose accumulation may saturate the absorption ability of the ground (Merz et al., 2021; Rentschler et al., 2022). On the opposite side of the spectrum, droughts often cause major economic disruptions through their impact on agriculture and can also have health impacts due to decreased water accessibility (especially in low-income countries), among other factors. Droughts are usually defined as a period of time during which there is a lack of, or abnormally low levels of, precipitation combined with extreme heat (Vicente-Serrano et al., 2020). Therefore, to study the potential impacts of precipitation-related extreme events, it is important to build statistical models that can accurately capture the behavior of precipitation intensities all the way from low values in the lower tail to high values in the upper tail, while also flexibly describing behavior in the bulk of the distribution.

From a statistical perspective, extreme events may be studied through the lens of extreme-value theory which characterizes the possible tail behaviors under certain regularity conditions (see, e.g., the books of Coles, 2001; Beirlant et al., 2004; Embrechts et al., 2013; de Carvalho et al., 2025). In the univariate framework, the generalized Pareto distribution plays a central role, being the only possible upper-tail limit of (properly rescaled) high threshold exceedances as the threshold increases arbitrarily (Davison and Smith, 1990). An

analogous representation can be obtained for the lower tail by symmetry, describing the behavior of extremely low threshold non-exceedances. When interest lies in both tails, a classical approach has thus been to fit the generalized Pareto distribution to extreme data from each tail separately; the fitted generalized Pareto distributions are then used for risk assessment by extrapolating further into the tails. While this approach has the benefit of being simple (under the assumption that appropriately chosen generalized Pareto distributed exceedances have been selected), it is based on the premise that the bulk of the distribution does not play an important role and that its analysis can be decoupled from that of (moderate) extremes. In practice, however, the bulk of the distribution often provides crucial information. Moreover, when two generalized Pareto distributions and another distribution are fitted separately to low extremes, high extremes and the bulk, respectively, a major drawback is to determine how to put these three pieces back together. The resulting bulk-tails mixture model will be discontinuous at the two chosen thresholds, which is an unwelcome artificial feature not present in the original data. In addition, threshold selection to define extreme events has always been a delicate issue in extreme-value theory (see, for example, the so-called “horror Hill plots” discussed in [Resnick and Stărică, 1997](#)). Assessing, both practically and theoretically, how threshold selection impacts downstream statistical inference is difficult ([Scarrott and MacDonald, 2012](#); [Alouini et al., 2026](#)). Sensitivity with respect to the threshold choice can be visually explored in the univariate context, but such ad-hoc visual devices (like mean-excess function and quantile-quantile plots) can become impractical in a multivariate context. In practice, the same quantile—e.g., the 95% percentile—is often arbitrarily chosen for all marginal variables (see, e.g., [Davison and Huser, 2015](#)).

To mitigate these practical issues, various modeling approaches have been proposed in the univariate case (see [Naveau, 2025](#), for a recent review). For positive random variables with a heavy upper tail, a first model proposed by [Frigessi et al. \(2002\)](#) was constructed as a mixture between a light-tailed distribution and a heavy-tailed one, with a dynamic weighting function designed to ensure that the former controls the bulk while the latter controls upper-tail extremes. Although conceptually appealing, such approaches are difficult to implement in practice, as the weight function parameters are difficult to estimate. Alternatively, [Carreau and Bengio \(2008, 2009\)](#) proposed to stitch a Pareto distribution with a Gaussian one in order

to obtain, within a neural network based approach, a flexible building block that handles both heavy tail behavior and the bulk, but the lower tail behavior was ignored. To comply with EVT on both sides of the distribution, [Naveau et al. \(2016\)](#) proposed a general class of models that includes simple parametric forms (see, e.g., [Papastathopoulos and Tawn, 2013](#)) and more complex semi-parametric models (see, e.g. [Tencaliec et al., 2020](#)). Such models have been used to model precipitation data (see, e.g., [Evin et al., 2018](#); [Gamet and Jalbert, 2022](#); [Haruna et al., 2023](#)), and similar constructions were proposed by [Stein \(2021a,b\)](#). In this work, we propose and study an extension of the so-called extended generalized Pareto distribution of [Naveau et al. \(2016\)](#) to the multivariate case. The main question is thus how to integrate multivariate EVT concepts into this new modeling framework, while keeping a flexible bulk, bypassing threshold selections, and enabling fast inference with our new model.

Most of the mathematical aspects of multivariate EVT are well established and can be found in the books of [Beirlant et al. \(2004\)](#) and [de Haan and Ferreira \(2006\)](#). Various applied treatments are covered by the recent handbook of [de Carvalho et al. \(2025\)](#). In particular, multivariate threshold exceedances are classically defined in terms of a norm and modeled with a multivariate generalized Pareto distribution (see, e.g., [Rootzén et al., 2018](#)). In this multivariate context, the choice of thresholds to define joint extremes not only remains a hurdle for practitioners, but it is even more complex than the univariate case. Furthermore, the computational burden when fitting multivariate generalized Pareto distributions using likelihood-based techniques increases rapidly with the dimension as classical censoring of marginally non-extreme observations make it very challenging. These two limitations have led to so-called subasymptotic models and to different inference strategies (see, e.g., [Morris et al., 2017](#); [Wadsworth et al., 2017](#); [Krupskii and Huser, 2022](#); [Shi et al., 2024](#)). These subasymptotic models seek to capture dependence not only at the highest possible quantiles, but also at lower intermediate levels, with flexible forms of tail decay (see, e.g., [Zhang et al., 2025](#)). A recurrent modeling strategy in many studies is to decompose the dataset at hand into radial and angular components. The radial part corresponds to a univariate projection, e.g., the L^1 -norm of all components, and a multivariate extreme event is defined when this radial vector is large. The angular part simply rescales the original dataset by the radial component. This representation leads to many different types of “scale-mixture” models. A

key hypothesis in multivariate EVT is to assume that the angle becomes independent of the radius as the latter becomes large. In such a framework, the interpretation is simple: the radius solely drives the upper tail behavior, while the angle entirely controls the dependence structure. The choice of the radial component (or more general “risk functionals”; see [de Fondeville and Davison, 2018](#)) and other considerations (e.g., hidden regular variation; see [Kulik and Soulier, 2020](#)) have led to a plethora of extremal models that can produce different types of extremal dependence structures (see, e.g., [Huser et al., 2017](#); [Engelke et al., 2019](#); [Wadsworth and Tawn, 2022](#); [Murphy-Barltrop et al., 2024](#); [Mackay and Jonathan, 2024](#); [Bacro et al., 2024](#); [Kakampakou et al., 2024](#); [Hazra et al., 2025](#)). In this work, we only focus on the most classical setup, the so-called asymptotic dependence case, which implies that multivariate extremes are strongly concomitant. As we require our multivariate extended generalized Pareto distribution to be compliant with multivariate EVT in both the upper and lower tails, two different angular components are needed. Depending on the value of the radial component, the upper (lower) extremal dependence is captured in our modeling framework by the upper (lower) angular component when the radius becomes large (small).

Our proposed model differs substantially from alternative approaches for blending the bulk with the tails without any threshold selection. For example, in the spirit of [Frigessi et al. \(2002\)](#), [Vrac et al. \(2007\)](#) proposed using a bivariate mixture model with a smooth dynamic weighting function. Similarly, [André et al. \(2024\)](#) used a weighted copula mixture model to blend bulk and tails, and [André and Tawn \(2025\)](#) proposed and studied a different copula model based on a mixture of Gaussian distributions. By contrast, in the present work, we move away from mixture distributions and instead propose a stochastic representation based on a weighted sum that integrates two angular components—one for the upper tail and the one for the lower tail—and where the weight of each term depends on the radial component. In other words, our proposed model is a dynamic mixture performed on the level of the stochastic representation, rather than the distribution or density function. Besides facilitating interpretation, another advantage of our construction is that it allows straightforward and fast simulation from the model. This opens the door to simulation-based-inference techniques that avoid costly likelihood-based computations. Precisely, we leverage recent amortized neural inference approaches ([Zammit-Mangion et al., 2025](#)), adapting both neural

point estimators and full posterior estimators to our context. More specifically, we deploy neural Bayes estimators (Sainsbury-Dale et al., 2024) to quickly get point estimates of model parameters, as well as normalizing flows to efficiently approximate the entire posterior distribution while bypassing costly Markov chain Monte Carlo sampling (Radev et al., 2020).

The paper is organized as follows. After recalling the basics of the univariate extended generalized Pareto distribution, Section 2 details our proposed multivariate model construction and some of its key properties. Section 3 details our neural inference approach, while Section 4 describes a simulation study conducted to compare its performance with more classical estimators. In Section 5, we illustrate our methodology (both the new model and the neural inference approach) with an application to daily rainfall times series data from the Netherlands over the years 1999–2024. Section 6 concludes with some discussion.

2. A multivariate extended generalized Pareto model

Section 2.1 recalls basics of the univariate extended generalized Pareto distribution; Section 2.2 extends it to the multivariate case, detailing the general construction of our novel multivariate model, and Section 2.3 studies its marginal and dependence properties in detail.

2.1. Univariate extended generalized Pareto distribution

In univariate extreme-value theory, the generalized Pareto distribution (GPD) is commonly used to model high threshold exceedances because it arises as the only possible non-degenerate limiting form, as the threshold tends to the upper endpoint of the distribution. More precisely, let $Y \sim F_Y$ be a random variable with upper endpoint y_U^* . If there exists a rescaling sequence $a_U(u) > 0$ such that

$$\mathbb{P}\left(\frac{Y - u}{a_U(u)} \leq y \mid Y > u\right) \rightarrow H_\xi(y/\sigma), \quad u \rightarrow y_U^*, \quad (1)$$

for some nondegenerate distribution $H_\xi(y/\sigma)$ and for some positive parameter σ , then the limit is the GPD with canonical form defined as

$$H_\xi(y) = \begin{cases} 1 - (1 + \xi y)^{-1/\xi}, & \xi \neq 0 \\ 1 - \exp(-y), & \xi = 0, \end{cases} \quad (2)$$

defined over the support $\{y > 0 : 1 + \xi y > 0\}$, where $\xi \in \mathbb{R}$ is a shape parameter, also known as the tail index. This asymptotic result motivates the use of $H_\xi(y/\sigma)$ as a model for unnormalized exceedances $Y - u \mid Y > u$ for high but finite thresholds u . Note that the scale parameter σ is meant to absorb the sequence $a_U(u)$, and thus may vary with u . In particular, if $\xi > 0$ and Y has an infinite upper endpoint, i.e., $y_U^* = \infty$, a simple expansion of (2) yields $\mathbb{P}(Y > y \mid Y > u) \approx (\xi y/\sigma)^{-1/\xi} = K_U y^{-1/\xi}$, as $y \rightarrow \infty$, for some constant $K_U > 0$. This implies that Y has a heavy, power-law upper-tail behavior.

Although the GPD in (1)–(2) characterizes the upper tail of Y , it also applies to the lower tail by symmetry. Precisely, if the limit

$$\mathbb{P}\left(\frac{v - Y}{a_L(v)} \leq y \mid Y < v\right) \rightarrow H_{\tilde{\xi}}(y/\tilde{\sigma}), \quad v \rightarrow y_L^*, \quad (3)$$

exists and is nondegenerate, where $a_L(v)$ is another positive rescaling sequence, then $H_{\tilde{\xi}}(y/\tilde{\sigma})$ is also a GPD of the form (2), yet with potentially different parameters $\tilde{\sigma} > 0, \tilde{\xi} \in \mathbb{R}$. A special case arises when Y is a positive random variable, in which case the lower bound of Y is $y_L^* = 0$. Suppose that for a fixed threshold $v \approx 0$, the distribution of $v - Y \mid Y < v$ is modeled using a GPD with scale $\tilde{\sigma} > 0$ and shape parameter $\tilde{\xi} < 0$. As the upper bound of the support is $-\tilde{\sigma}/\tilde{\xi} = v$, this implies that $\tilde{\xi} = -\tilde{\sigma}/v$. Therefore, in this case, we see that the distribution of low values of Y can be modeled as $Y \mid Y < v \sim (y/v)^{v/\tilde{\sigma}} \sim K_L y^\kappa$, for some constant $K_L > 0$ and lower-tail shape parameter $\kappa = -1/\tilde{\xi} = v/\tilde{\sigma} > 0$.

To link both tail behaviors together with a smooth transition in between, one can consider the extended generalized Pareto distribution (eGPD). This name was originally coined by [Papastathopoulos and Tawn \(2013\)](#) with the objective of improving upper tail modeling (subasymptotic large extremes). To integrate the lower tail behavior (subasymptotic low extremes) into the eGPD class, [Naveau et al. \(2016\)](#) proposed an extension to capture the full range of nonnegative variables. This updated eGPD has the general form $F_Y(y) = B\{H_\xi^\kappa(y/\sigma)\}$, where $H_\xi(\cdot)$ is the GPD with shape parameter ξ defined in (2), σ is a positive scale parameter, and $B : [0, 1] \rightarrow [0, 1]$ is any continuous cumulative distribution function over the interval $[0, 1]$ with positive derivatives at 0 and 1, i.e., $B'(0) > 0$ and $B'(1) > 0$, to make sure that the upper and lower tails are driven by κ and ξ , respectively. The most

parsimonious case is to set $B(u) = u$, in which case the eGPD can be expressed as

$$F_Y(y) = \begin{cases} \{1 - (1 + \xi y/\sigma)^{-1/\xi}\}^\kappa, & \xi \neq 0 \\ \{1 - \exp(-y/\sigma)\}^\kappa, & \xi = 0. \end{cases} \quad (4)$$

When $\xi > 0$, it is easy to verify that $1 - F_Y(y) \sim \kappa(\xi y/\sigma)^{-1/\xi}$, as $y \rightarrow \infty$, and that $F_Y(y) \sim (y/\sigma)^\kappa$, as $y \rightarrow 0$. Therefore, this three-parameter eGPD complies with EVT in both tails, with κ a shape parameter controlling the lower tail behavior, ξ a shape parameter controlling the upper tail behavior, and σ an overall scale parameter affecting the whole distribution from low to high quantiles. While more flexible extensions of this simple eGPD have been proposed by [Tencaliec et al. \(2020\)](#) and other types of smooth bulk–tail models have been proposed by [Stein \(2021a,b\)](#) and [Yadav et al. \(2021, 2022\)](#) among others, the simple form (4) has found interest in a wide range of environmental applications ([Le Gall et al., 2022](#); [Yadav et al., 2023, 2025](#); [Haruna et al., 2024](#); [Cisneros et al., 2024](#)).

2.2. General construction of the multivariate eGPD model

In the sequel, a vector of dimension d is denoted by $\mathbf{x} = (x_1, \dots, x_d)^\top$. The bold symbol $\mathbf{0}$ refers to a vector all elements of which are equal to 0. Operations between vectors are to be understood componentwise. For instance, if $\mathbf{x} = (x_1, \dots, x_d)^\top$ and $\mathbf{y} = (y_1, \dots, y_d)^\top$, then \mathbf{xy} is the vector with components $x_j y_j$, $j = 1, \dots, d$. Similarly, \mathbf{x}^{-1} is the vector with components x_j^{-1} , $j = 1, \dots, d$. The L^1 norm of vector \mathbf{x} will be denoted by $\|\mathbf{x}\|_1 = \sum_{j=1}^d |x_j|$.

To extend the eGPD in (4) to the multivariate case, we specify its stochastic representation. Having the modeling of precipitation in mind, let $R \sim F_R$ be a positive random variable distributed according to the univariate eGPD (4) with $\xi > 0$ (i.e., with a heavy upper tail), which will be closely linked to the random vector’s marginal behavior. To control dependence in the lower and upper tails, respectively, let $\mathbf{L} = (L_1, \dots, L_d)^\top$ and $\mathbf{U} = (U_1, \dots, U_d)^\top$ be (nondegenerate) positive random vectors lying on the L^1 -sphere (i.e., the “simplex”), i.e., one has $L_j, U_j \in [0, 1]$ such that $\mathbb{P}(L_j > 0) = \mathbb{P}(U_j > 0) = 1$ for all $j = 1, \dots, d$, and $\|\mathbf{L}\|_1 = \|\mathbf{U}\|_1 = 1$. Assume that R , \mathbf{L} , and \mathbf{U} are mutually independent. Our proposed

multivariate eGPD is then defined through the construction

$$\mathbf{Y} = R \left([1 - \omega\{F_R(R)\}]\mathbf{L} + \omega\{F_R(R)\}\mathbf{U} \right), \quad (5)$$

where $\omega : [0, 1] \rightarrow [0, 1]$ is a continuous cumulative distribution function defined over the interval $[0, 1]$ (i.e., non-decreasing, $\lim_{u \downarrow 0} \omega(u) = 0$, and $\lim_{u \uparrow 1} \omega(u) = 1$) controlling the weight attributed to the vectors \mathbf{L} (lower tail) and \mathbf{U} (upper tail) in the dynamic weighted sum (5). Intuitively, as both \mathbf{L} and \mathbf{U} are on the sphere and the weight function $\omega(\cdot)$ is bounded in $[0, 1]$, marginal properties of the random vector \mathbf{Y} will be mostly dictated by R . Moreover, since $\omega\{F_R(R)\} \approx 1$ for large realizations of R , the vector \mathbf{U} will essentially control the upper tail dependence structure. Conversely, since $\omega\{F_R(R)\} \approx 0$ for realizations of R close to zero, the vector \mathbf{L} will control the lower tail dependence structure. This is formalized in the next section, where we explore the model properties in more detail. We also note that while we could choose other norms (or even “risk functionals”; [de Fondeville and Davison, 2018](#)) than the L^1 norm, the model (5) already provides a fairly flexible framework.

2.3. Properties of the multivariate eGPD model

2.3.1. Moments

While marginal distributions are generally intractable, the marginal moments of each component Y_j (provided they exist) may be expressed from the model definition in (5) as

$$\mathbb{E}(Y_j^q) = \sum_{l=0}^q \binom{q}{l} \mathbb{E}\left\{R^q(1 - \omega_R)^l \omega_R^{q-l}\right\} \mathbb{E}(L_j^l) \mathbb{E}(U_j^{q-l}), \quad q = 1, 2, \dots, \quad (6)$$

where $\omega_R = \omega\{F_R(R)\}$. As $\|\mathbf{L}\|_1 = \|\mathbf{U}\|_1 = 1$, one always has $\mathbb{E}(L_j^l) < 1$ and $\mathbb{E}(U_j^{q-l}) < 1$, and the existence of the q -th moment in (6) will therefore depend on the existence of $\mathbb{E}\{R^q(1 - \omega_R)^l \omega_R^{q-l}\}$, $l = 0, \dots, q$. Since $\omega(u) \in [0, 1]$, a sufficient condition for it is the finiteness of $\mathbb{E}(R^q)$, and as R is an eGPD, this is ensured with $\xi < 1/q$. Similarly, when $\xi < 1/2$, the covariance structure of \mathbf{Y} can also straightforwardly be obtained as

$$\begin{aligned} \text{Cov}(Y_j, Y_k) &= \mathbb{E}\{R^2(1 - \omega_R)^2\} \mathbb{E}(L_j L_k) + \mathbb{E}\{R^2(1 - \omega_R)\omega_R\} \mathbb{E}(L_j) \mathbb{E}(U_k) \\ &\quad + \mathbb{E}\{R^2(1 - \omega_R)\omega_R\} \mathbb{E}(L_k) \mathbb{E}(U_j) + \mathbb{E}(R^2 \omega_R^2) \mathbb{E}(U_j U_k) \end{aligned}$$

$$\begin{aligned}
& - \mathbb{E}\{R(1 - \omega_R)\}^2 \mathbb{E}(L_j) \mathbb{E}(L_k) - \mathbb{E}\{R(1 - \omega_R)\} \mathbb{E}(\omega_R) \mathbb{E}(L_j) \mathbb{E}(U_k) \\
& - \mathbb{E}\{R(1 - \omega_R)\} \mathbb{E}(\omega_R) \mathbb{E}(L_k) \mathbb{E}(U_j) - \mathbb{E}(R\omega_R)^2 \mathbb{E}(U_j) \mathbb{E}(U_k), \quad j, k = 1, \dots, d. \quad (7)
\end{aligned}$$

As with the marginal moments, the covariance cannot be expressed in closed form in full generality, but it can be easily approximated by numerical simulations. Equations (6) and (7) also reveal that all model components, i.e., R , \mathbf{L} and \mathbf{U} , jointly affect the marginal moments and covariance behavior of \mathbf{Y} in a non-trivial way.

2.3.2. Upper and lower tail behaviors

To understand the (upper or lower) tail structure of \mathbf{Y} , first note that

$$\|\mathbf{Y}\|_1 = R([1 - \omega\{F_R(R)\}]\|\mathbf{L}\|_1 + \omega\{F_R(R)\}\|\mathbf{U}\|_1) = R, \quad (8)$$

given that $\|\mathbf{L}\|_1 = \|\mathbf{U}\|_1 = 1$ by definition. Therefore, the L^1 -norm of \mathbf{Y} is exactly determined by the random variable R .

To get a first glimpse into the upper and lower tail dependence structure of \mathbf{Y} , it is natural to consider a “radial-angular” decomposition. Treating $\|\mathbf{Y}\|_1 = R$ as the “radius”, the “angle” is obtained as $\mathbf{Y}/\|\mathbf{Y}\|_1 = [1 - \omega\{F_R(R)\}]\mathbf{L} + \omega\{F_R(R)\}\mathbf{U}$. Hence, since $\omega(u) \downarrow 0$ as $u \downarrow 0$ and $\omega(u) \uparrow 1$ as $u \uparrow 1$, and with R , \mathbf{L} and \mathbf{U} being independent, it follows that

$$\begin{aligned}
\mathbb{P}(\mathbf{Y}/\|\mathbf{Y}\|_1 \leq \mathbf{u} \mid \|\mathbf{Y}\|_1 > r) &\rightarrow \mathbb{P}(\mathbf{U} \leq \mathbf{u}), & r \rightarrow \infty; \\
\mathbb{P}(\mathbf{Y}/\|\mathbf{Y}\|_1 \leq \mathbf{l} \mid \|\mathbf{Y}\|_1 < r) &\rightarrow \mathbb{P}(\mathbf{L} \leq \mathbf{l}), & r \rightarrow 0.
\end{aligned}$$

In other words, the (angular) dependence structure of “high extremes” and “low extremes” of \mathbf{Y} , when defined in terms of the L^1 -norm (being large or small), are completely determined by the vectors \mathbf{U} and \mathbf{L} , respectively.

More detailed theoretical insights can be achieved through the lens of regular variation and related tools, such as Breiman’s Lemma (Breiman, 1965) and extensions thereof (see, e.g., Fougères and Mercadier, 2012). In the univariate case, a random variable X is said to be regularly varying with index $\alpha > 0$, scaling sequence $a(t) > 0$ and limit measure ν if $t\mathbb{P}(X/a(t) \in \cdot) \xrightarrow{v} \nu(\cdot)$, as $t \rightarrow \infty$, where \xrightarrow{v} denotes the vague convergence of measures

(i.e., convergence holds for all compact Borel sets with boundary of measure zero). The scaling sequence can always be taken as $a(t) = t^{1/\alpha}$, and because the limit measure ν is then necessarily homogeneous of order $-\alpha$, i.e., $\nu(tA) = t^{-\alpha}\nu(A)$ for all $t > 0$ and Borel sets A , the upper tail of X can therefore be characterized as $\mathbb{P}(X > x) \sim \nu((1, \infty))x^{-\alpha}$ as $x \rightarrow \infty$. This implies that the random variable X is heavy-tailed with tail index $\xi = 1/\alpha$.

Similarly, in the multivariate case, a random vector \mathbf{X} is said to be (multivariate) regularly varying with index $\alpha > 0$, scaling sequence $a(t) > 0$ and limit measure ν if $t\mathbb{P}(\mathbf{X}/a(t) \in \cdot) \xrightarrow{\nu} \nu(\cdot)$, as $t \rightarrow \infty$, where similar properties hold for $a(t)$ and ν . Intuitively, multivariate regular variation characterizes random vectors that are (both marginally and jointly) heavy-tailed and asymptotically dependent. Furthermore, if \mathbf{X} is multivariate regularly varying, then it is in the max-domain of attraction of a max-stable random vector with (heavy-tailed) Fréchet marginals (see, e.g., [Resnick, 1987](#), for further details on regular variation and extreme-value theory).

Upper tail. To study the upper tail of \mathbf{Y} in our setting, we can equivalently study the upper tail of $R\mathbf{U}$ (since $\omega(u) \uparrow 1$ as $u \uparrow 1$). Note that R follows a heavy-tailed eGPD with $\xi > 0$, so it is regularly varying with index $\alpha_R = 1/\xi > 0$, scaling sequence $a_R(t) = t^\xi$ and limit measure $\nu_R((r, \infty)) = \kappa(\sigma/\xi)^{1/\xi}r^{-1/\xi}$ for all $r > 0$. Further, given $\|\mathbf{U}\|_1 = 1$, each component U_j automatically meets the condition that there exists $\varepsilon > 0$ such that $0 < \mathbb{E}(U_j^{1/\xi+\varepsilon}) < \infty$; in fact, this holds for all $\varepsilon > 0$ as $|U_j| \leq 1$. According to Breiman's Lemma (see [Breiman, 1965](#)), RU_j is also regularly varying with the same index $\alpha_{RU_j} = \alpha_R = 1/\xi$ and scaling sequence $a_{RU_j}(t) = a_R(t) = t^\xi$, but with a modified limiting measure: $\nu_{RU_j}((r, \infty)) = \mathbb{E}(U_j^{1/\xi})\nu_R((r, \infty))$. Thus, the marginal upper tail of Y_j behaves as

$$\mathbb{P}(Y_j > y) \sim \mathbb{P}(RU_j > y) \sim \mathbb{E}(U_j^{1/\xi})\kappa(\sigma/\xi)^{1/\xi}y^{-1/\xi}, \quad y \rightarrow \infty.$$

Hence, Y_j is heavy-tailed in the upper tail with the same tail index as the random variable R , but its scale is modified through the random variable U_j .

The joint upper tail of the vector \mathbf{Y} can similarly be studied through a multivariate extension of Breiman's Lemma. Note that one can write $R\mathbf{U} = \mathbf{R}\mathbf{U}$, where $\mathbf{R} = (R, \dots, R)^\top$ is a fully dependent d -dimensional random vector that is multivariate regularly-varying

with index $\alpha_{\mathbf{R}} = 1/\xi$, scaling sequence $a_{\mathbf{R}}(t) = t^\xi$ and limit measure $\nu_{\mathbf{R}}([\mathbf{0}, \mathbf{r}]^C) = \max(r_1^{-1/\xi}, \dots, r_d^{-1/\xi})\kappa(\sigma/\xi)^{1/\xi}$, $\mathbf{r} = (r_1, \dots, r_d)^\top$, with A^C the complement of the set A . Thus, thanks to Theorem 3 of [Fougères and Mercadier \(2012\)](#), $\mathbf{R}\mathbf{U}$ is also multivariate regularly-varying with the same index and scaling sequence, but with limiting measure

$$\begin{aligned}\nu_{\mathbf{R}\mathbf{U}}([\mathbf{0}, \mathbf{r}]^C) &= \mathbb{E}\{\nu_{\mathbf{R}}(\mathbf{U}^{-1}[\mathbf{0}, \mathbf{r}]^C)\} = \mathbb{E}\{\nu_{\mathbf{R}}([\mathbf{0}, \mathbf{r}\mathbf{U}^{-1}]^C)\} \\ &= \mathbb{E}\left[\max\left\{(r_1/U_1)^{-1/\xi}, \dots, (r_d/U_d)^{-1/\xi}\right\}\right]\kappa(\sigma/\xi)^{1/\xi}.\end{aligned}$$

This implies that the joint upper tail of \mathbf{Y} can be characterized by

$$\begin{aligned}\mathbb{P}(\mathbf{Y} \in t[\mathbf{0}, \mathbf{y}]^C) &\sim \mathbb{P}(\mathbf{R}\mathbf{U} \in t[\mathbf{0}, \mathbf{y}]^C) \sim \nu_{\mathbf{R}\mathbf{U}}([\mathbf{0}, t\mathbf{y}]^C) \\ &= \mathbb{E}\left[\max\left\{(y_1/U_1)^{-1/\xi}, \dots, (y_d/U_d)^{-1/\xi}\right\}\right]\kappa(\sigma/\xi)^{1/\xi}t^{-1/\xi}, \quad t \rightarrow \infty.\end{aligned}$$

From this expression, we see how \mathbf{U} modulates the joint upper tail structure of \mathbf{Y} .

Lower tail. To study the lower tail of \mathbf{Y} in our setting, we can similarly study the lower tail of $\mathbf{R}\mathbf{L}$ (since $\omega(u) \downarrow 0$ as $u \downarrow 0$) or, equivalently, characterize the upper tail behavior of $\mathbf{R}^{-1}\mathbf{L}^{-1}$. Note that \mathbf{R}^{-1} is regularly-varying with index $\alpha_{\mathbf{R}^{-1}} = \kappa$, scaling sequence $a_{\mathbf{R}^{-1}}(t) = t^{1/\kappa}$, and limit measure $\nu_{\mathbf{R}^{-1}}((r, \infty)) = \sigma^{-\kappa}r^{-\kappa}$. Two main cases can arise given that \mathbf{L}^{-1} is not necessarily upper-bounded nor lighter tailed than \mathbf{R}^{-1} : (i) the first case arises when each component L_j meets the condition that there exists $\varepsilon > 0$ such that $\mathbb{E}(L_j^{-(\kappa+\varepsilon)}) < \infty$, $j = 1, \dots, d$. This is trivially true when L_j is lower bounded (i.e., $L_j > \delta > 0$ for some $\delta > 0$, almost surely). Then, Breiman's Lemma and its multivariate extension imply that the marginal and joint lower tail of \mathbf{Y} behave, respectively, as

$$\mathbb{P}(Y_j \leq y) \sim \mathbb{P}(\mathbf{R}^{-1}L_j^{-1} > y^{-1}) \sim \mathbb{E}(L_j^{-\kappa})\sigma^{-\kappa}y^\kappa, \quad y \rightarrow 0; \quad (9)$$

$$\begin{aligned}\mathbb{P}(\mathbf{Y} \in t[\mathbf{y}, \infty)^C) &\sim \mathbb{P}(\mathbf{R}^{-1}\mathbf{L}^{-1} \in t^{-1}[\mathbf{0}, \mathbf{y}^{-1}]^C) \\ &\sim \mathbb{E}\left[\max\left\{(y_1/L_1)^\kappa, \dots, (y_d/L_d)^\kappa\right\}\right]\sigma^{-\kappa}t^\kappa, \quad t \rightarrow 0.\end{aligned} \quad (10)$$

Thus, in this case, Y_j has the same lower tail index as \mathbf{R} itself, but its scale is modified through the random variable L_j . Furthermore, the random vector \mathbf{L} modulates the joint

lower tail dependence structure of \mathbf{Y} . (ii) The second case arises when \mathbf{L}^{-1} is multivariate regularly varying with index $\alpha_{\mathbf{L}^{-1}} > 0$ and heavier-tailed than R^{-1} , i.e., $\alpha_{\mathbf{L}^{-1}} < \kappa$ such that $\mathbb{E}(R^{-\alpha_{\mathbf{L}^{-1}} + \varepsilon}) < \infty$ for some $\varepsilon > 0$. Then, using Breiman’s Lemma and its multivariate extension, the marginal and joint lower tail structure of \mathbf{Y} can be written, respectively, as

$$\mathbb{P}(Y_j \leq y) \sim \mathbb{P}(R^{-1}L_j^{-1} > y^{-1}) \sim \mathbb{E}(R^{-\alpha_{\mathbf{L}^{-1}}})\nu_{L_j^{-1}}((1, \infty))y^{\alpha_{\mathbf{L}^{-1}}}, \quad y \rightarrow 0; \quad (11)$$

$$\mathbb{P}(\mathbf{Y} \in t[\mathbf{y}, \infty)^C) \sim \mathbb{P}(\mathbf{R}^{-1}\mathbf{L}^{-1} \in t^{-1}[\mathbf{0}, \mathbf{y}^{-1}]^C) \sim \mathbb{E}\{\nu_{\mathbf{L}^{-1}}([\mathbf{0}, R\mathbf{y}^{-1}]^C)\}t^{\alpha_{\mathbf{L}^{-1}}}, \quad t \rightarrow 0. \quad (12)$$

where $\nu_{L_j^{-1}}$ and $\nu_{\mathbf{L}^{-1}}$ denote the limit measures of L_j^{-1} and \mathbf{L}^{-1} , respectively. Therefore, in this case, the marginal lower tail of \mathbf{Y} is dictated by the tail index of \mathbf{L}^{-1} , which also controls the lower tail dependence structure through its limit measure.

3. Inference

We now outline several parameter inference methods used with the proposed model. In Section 3.1, we outline a classical likelihood–method-of-moments approach. In Section 3.2, we describe two likelihood-free, neural-network-based approaches: neural Bayes estimation (e.g., [Sainsbury-Dale et al., 2024](#)) and neural posterior estimation (e.g., [Radev et al., 2020](#)). Throughout, we assume that each model component has its own set of parameters, denoted by $\boldsymbol{\theta}_R$ for R , $\boldsymbol{\theta}_L$ for \mathbf{L} , and $\boldsymbol{\theta}_U$ for \mathbf{U} . The weight function $\omega(\cdot)$ also has its own set of parameters, $\boldsymbol{\theta}_\omega$, and we write $\boldsymbol{\theta} = (\boldsymbol{\theta}_R^\top, \boldsymbol{\theta}_L^\top, \boldsymbol{\theta}_U^\top, \boldsymbol{\theta}_\omega^\top)^\top$ to denote all model parameters. Let $\mathbf{y}_1, \dots, \mathbf{y}_n$ be independent and identically distributed realizations of a random vector \mathbf{Y} drawn from the model (5). Let F_R , F_L , F_U , and F_Y be the cumulative distribution functions corresponding to R , \mathbf{L} , \mathbf{U} , and \mathbf{Y} , respectively. Furthermore, assume that all model components admit densities, and denote them by f_R , f_L , f_U , and f_Y , respectively.

3.1. Hybrid likelihood–moment estimators

As a full likelihood estimation will involve the intractable data density f_Y , the inference presented in this section has to be hybrid, in the sense that some parameters will be estimated by likelihood maximization while other parameters will be inferred with a method-of-moment approach. Hence, this hybrid approach does not offer all the nice optimality properties of

full likelihood estimators. Still, it can be viewed as a benchmark with respect to the neural inference methods presented in Section 3.2.

Here, we exploit that the latent components R , \mathbf{L} and \mathbf{U} can be indirectly “observed”. As noted in (8), $\|\mathbf{Y}\|_1 = R \sim F_R$. Therefore, the parameter $\boldsymbol{\theta}_R$ can be estimated via maximum likelihood using the statistics $\|\mathbf{y}_i\|_1$, $i = 1, \dots, n$, by maximizing the function:

$$\mathcal{L}(\boldsymbol{\theta}_R) = \prod_{i=1}^n f_R(\|\mathbf{y}_i\|_1; \boldsymbol{\theta}_R).$$

This yields the estimate $\hat{\boldsymbol{\theta}}_R^{\text{MLE}}$. Next, since F_L (or F_U) characterizes the asymptotic distribution of the angles $\mathbf{Y}/\|\mathbf{Y}\|_1$ given that the radius $\|\mathbf{Y}\|_1$ converges to zero (or infinity), one can set a low threshold r_0^L (or high threshold r_0^U), extract low (or high) extremes from the dataset, and maximize the corresponding likelihood function. Specifically, define the index sets $\mathcal{I}_L = \{i = 1, \dots, n : \|\mathbf{y}_i\|_1 < r_0^L\}$ and $\mathcal{I}_U = \{i = 1, \dots, n : \|\mathbf{y}_i\|_1 > r_0^U\}$. One can estimate $\boldsymbol{\theta}_L$ and $\boldsymbol{\theta}_U$ by maximizing, respectively,

$$\mathcal{L}(\boldsymbol{\theta}_L) = \prod_{i \in \mathcal{I}_L} f_L(\mathbf{y}_i/\|\mathbf{y}_i\|_1; \boldsymbol{\theta}_L), \quad \text{and} \quad \mathcal{L}(\boldsymbol{\theta}_U) = \prod_{i \in \mathcal{I}_U} f_U(\mathbf{y}_i/\|\mathbf{y}_i\|_1; \boldsymbol{\theta}_U).$$

This yields the estimates $\hat{\boldsymbol{\theta}}_L^{\text{MLE}}$ and $\hat{\boldsymbol{\theta}}_U^{\text{MLE}}$, respectively. Estimating $\boldsymbol{\theta}_\omega$ is more difficult, as the weight function $\omega(\cdot)$ affects the entire distribution from low to high quantiles and there is no general closed-form likelihood function that can be used to estimate it. However, as $\omega(\cdot)$ mostly affects the bulk of the distribution, a method-of-moments approach might be reasonable. As seen in (6) and (7), the weight function affects all moments. Estimators based on moments may thus be obtained by solving a system of equations—whose number should equal the number of parameters in $\boldsymbol{\theta}_\omega$ —selected among the following ones:

$$\text{MOM}_q(\boldsymbol{\theta}_\omega) = \sum_{j=1}^d \left(\mathbb{E}(Y_j^q) - \bar{y}_{\cdot j}^q \right)^2 = 0, \quad q = 1, 2, \dots; \quad (13)$$

$$\text{MOM}_{\text{cov}}(\boldsymbol{\theta}_\omega) = \sum_{j=1}^d \sum_{k=1}^d \left(\text{Cov}(Y_j, Y_k) - \frac{1}{n-1} \sum_{i=1}^n (y_{ij} - \bar{y}_{\cdot j})(y_{ik} - \bar{y}_{\cdot k}) \right)^2 = 0, \quad (14)$$

where y_{ij} is the j -th component of realization \mathbf{y}_i , and $\bar{y}_{\cdot j}^q = n^{-1} \sum_{i=1}^n y_{ij}^q$ is the q -th sample

moment of the j -th component (with $\bar{y}_{\cdot j} \equiv \overline{y_{\cdot j}^1}$ for the sample mean). The theoretical counterparts, denoted by $\mathbb{E}(Y_j^q)$ for the marginal moments and $\text{Cov}(Y_j, Y_k)$ for the covariances, are computed from (6) and (7), respectively, under parameter $\boldsymbol{\theta}_\omega$ (that we wish to estimate) and the true parameters $\boldsymbol{\theta}_R, \boldsymbol{\theta}_L, \boldsymbol{\theta}_U$ (that are fixed when solving (13) and/or (14)). In practice, these true values are unknown and may be replaced with their likelihood-based estimates, $\hat{\boldsymbol{\theta}}_R^{\text{MLE}}, \hat{\boldsymbol{\theta}}_L^{\text{MLE}}, \hat{\boldsymbol{\theta}}_U^{\text{MLE}}$ obtained in a first step. As the theoretical moments often do not have closed-form expressions, we approximate them by Monte Carlo (i.e., sample moments) using a large simulation sample with parameters fixed to $\hat{\boldsymbol{\theta}}_R^{\text{MLE}}, \hat{\boldsymbol{\theta}}_L^{\text{MLE}}, \hat{\boldsymbol{\theta}}_U^{\text{MLE}}, \boldsymbol{\theta}_\omega$. This simulated method-of-moments-based approach (McFadden, 1989) yields the estimate $\hat{\boldsymbol{\theta}}_\omega^{\text{MOM}}$.

While providing valid inference, the estimators described above each rely on partial information: $\hat{\boldsymbol{\theta}}_R^{\text{MLE}}$ uses only a scalar summary of \mathbf{Y} (i.e., its L^1 -norm), while $\hat{\boldsymbol{\theta}}_L^{\text{MLE}}$ and $\hat{\boldsymbol{\theta}}_U^{\text{MLE}}$ each exploit information from one tail only. Further, the latter also rely on an asymptotic characterization of the lower or upper tails, respectively, and they will thus be subject to some bias if the thresholds r_0^L and r_0^U are not set sufficiently low and high, respectively. The estimator $\hat{\boldsymbol{\theta}}_\omega^{\text{MOM}}$, meanwhile, is based on moments rather than the likelihood function, and may therefore suffer from reduced statistical efficiency. This motivates the development of alternative inference methods that better utilize the full information contained in the data.

3.2. Neural estimators

To improve inference and estimate all parameters simultaneously using the full information available in the data, while also facilitating uncertainty assessment, a modern possible avenue is to use neural simulation-based inference approaches (Zammit-Mangion et al., 2025). Such approaches are “likelihood-free”, in the sense that they do not require the computation of any likelihood function. They are also “amortized”, in the sense that the entire computational cost is encapsulated in the initial training phase: once the neural network is trained using simulated data (usually a few hours), inference with observed data is extremely fast, and the trained neural network can be reused repeatedly with new data from the same model at almost no computational cost (usually a few milliseconds).

One such approach uses neural networks to approximate Bayes estimators, which are functionals (point summaries) of the posterior distribution. These *neural Bayes estimators*

(NBEs; e.g., [Sainsbury-Dale et al., 2024](#); [Richards et al., 2025](#); [André et al., 2025](#)) are presented in Section 3.2.1. Alternatively, one can approximate the entire posterior distribution using *neural posterior estimators* (NPEs; e.g., [Radev et al., 2020](#)), discussed in Section 3.2.2.

Before proceeding, we outline some fundamental elements common to both methods. Both approaches involve sampling a large set $\{\boldsymbol{\theta}^{(k)}\}_{k=1}^K$ of parameter vectors from a prior distribution $p(\boldsymbol{\theta})$, simulating corresponding datasets $\{\mathbf{y}_1^{(k)}, \dots, \mathbf{y}_n^{(k)}\}_{k=1}^K$ of conditionally independent draws from the model given each $\boldsymbol{\theta}^{(k)}$, and training a neural network using these parameter–data pairs. To enable amortized inference, where the neural network is trained once and then reused with negligible cost for new datasets from the same model, the prior $p(\boldsymbol{\theta})$ must be vague enough to cover all possible scenarios in which the neural network may be applied. However, as the prior becomes more vague, both the number K of required simulations and the expressiveness needed from the network tend to increase: a balance is therefore necessary between applicability across different datasets and computational efficiency.

3.2.1. Neural Bayes estimators

An NBE for the parameter $\boldsymbol{\theta} \in \Theta$ of a parametric statistical model (such as our model in (5)), defined on a sample space \mathcal{S} , is constructed as follows. Let $\hat{\boldsymbol{\theta}}_\gamma : \mathcal{S}^n \rightarrow \Theta$ denote a neural network parameterized by γ , that maps n data replicates as input into parameter estimates as output. Note that the neural-network parameters γ are often referred to as “weights” and “biases” in the machine-learning literature. Then, an NBE is obtained by solving

$$\hat{\gamma} = \arg \min_{\gamma} \sum_{k=1}^K \ell\{\boldsymbol{\theta}^{(k)}, \hat{\boldsymbol{\theta}}_\gamma(\mathbf{y}_1^{(k)}, \dots, \mathbf{y}_n^{(k)})\}, \quad (15)$$

where $\ell(\cdot, \cdot)$ is a user-specified loss function, such as the L^1 (absolute) loss $\ell(\boldsymbol{\theta}, \hat{\boldsymbol{\theta}}) = \|\boldsymbol{\theta} - \hat{\boldsymbol{\theta}}\|_1$ or the L^2 (quadratic) loss $\ell(\boldsymbol{\theta}, \hat{\boldsymbol{\theta}}) = \|\boldsymbol{\theta} - \hat{\boldsymbol{\theta}}\|_2^2$. The process of performing the optimization task (15) is referred to as “training the network”, and this can be done efficiently using back-propagation and stochastic gradient descent. Once trained, the NBE $\hat{\boldsymbol{\theta}}_{\hat{\gamma}}(\cdot)$ can be used by “plugging in” any realization $\mathbf{y}_1, \dots, \mathbf{y}_n$ observed from the same statistical model, yielding point estimates at almost no computational cost.

Although NBEs leverage deep learning and are sometimes referred to as “black-box es-

timators,” they are firmly grounded in statistical decision theory. Specifically, the objective function in (15) is a Monte Carlo approximation of the Bayes risk,

$$r(\hat{\boldsymbol{\theta}}(\cdot)) = \int_{\Theta} \left\{ \int_{S^n} \ell(\boldsymbol{\theta}, \hat{\boldsymbol{\theta}}(\mathbf{y}_1, \dots, \mathbf{y}_n)) \prod_{i=1}^n f_{\mathbf{Y}}(\mathbf{y}_i | \boldsymbol{\theta}) d\mathbf{y}_1 \cdots d\mathbf{y}_n \right\} p(\boldsymbol{\theta}) d\boldsymbol{\theta}, \quad (16)$$

and NBEs therefore approximate Bayes estimators (minimizers of (16)), which lends them a principled interpretation. In particular, Bayes estimators are functionals of the posterior distribution induced by the prior $p(\boldsymbol{\theta})$, with the specific functional determined by the choice of loss function $\ell(\cdot, \cdot)$. For instance, the L^2 and L^1 loss functions yield the posterior mean and the vector of marginal posterior medians, respectively. These estimators enjoy appealing asymptotic properties under mild conditions (e.g., consistency, efficiency; see Casella and Berger, 2001). Moreover, since neural networks are universal function approximators (Hornik et al., 1989), an NBE based on a sufficiently flexible neural network can approximate the true Bayes estimator arbitrarily well as the number K of simulations in (15) increases; see Rödder et al. (2025) for theoretical results of consistency under regularity conditions and the L^2 loss. Therefore, it is unsurprising that NBEs have demonstrated strong empirical performance in practice (e.g., Sainsbury-Dale et al., 2024; André et al., 2025).

Choosing an appropriate architecture (i.e., functional form) for the neural network is key and strongly depends on the structure of the data. In our case, we are interested in making inference for the multivariate model (5) observed with multiple independent replicates. Following Sainsbury-Dale et al. (2024), we use the DeepSets architecture (Zaheer et al., 2017), which appropriately handles exchangeable data by imposing permutation invariance of the replicates. This architecture may be written as

$$\hat{\boldsymbol{\theta}}_{\boldsymbol{\gamma}}(\mathbf{y}_1, \dots, \mathbf{y}_n) = \boldsymbol{\phi} \left\{ \frac{1}{n} \sum_{i=1}^n \boldsymbol{\psi}(\mathbf{y}_i), \log(n) \right\}, \quad (17)$$

where $\boldsymbol{\phi}$ and $\boldsymbol{\psi}$ are neural networks themselves (with $\boldsymbol{\gamma}$ combining their parameters). The role of the inner neural network $\boldsymbol{\psi}$ is to (automatically) extract informative summary statistics, which are then optimally mapped, together with the sample size n on log-scale, to parameter estimates via the outer neural network $\boldsymbol{\phi}$. In the multivariate case, since there is a priori no

spatial, temporal, or graphical structure in the data that can be exploited, it is natural to choose both ϕ and ψ as standard dense multilayer perceptrons (MLPs) as in [André et al. \(2025\)](#), [Coloma and Kleiber \(2025\)](#), and [Sainsbury-Dale et al. \(2025b\)](#), Section S6). The DeepSets architecture can accommodate datasets of different sizes, n , but the NBE may not perform well with data that have not been “seen” during training. Thus, to make the NBE applicable to varying sample sizes, it is important to randomize the sample size n during training alongside the model parameters and the data. This slightly changes the objective functions in (15) and (16), but the principle remains the same.

Uncertainty assessment with NBEs proceeds naturally using bootstrap techniques (e.g., [Lenzi et al., 2023](#); [Richards et al., 2025](#); [Sainsbury-Dale et al., 2024](#)), which are particularly attractive when nonparametric bootstrap is possible (e.g., when the data consist of independent replicates), or when simulation from the fitted model is fast, in which case parametric bootstrap is also computationally efficient. Alternatively, one may construct an NBE that approximates a set of marginal posterior quantiles, which can then be used to construct credible intervals for each parameter ([Sainsbury-Dale et al., 2025a](#); [André et al., 2025](#)). Inference then remains fully amortized since, once the NBEs are trained, both point estimates and credible intervals can be obtained with virtually zero computational cost.

3.2.2. Neural posterior estimators

We now describe NPEs, which allow for amortized approximate posterior inference through the minimization of an expected Kullback–Leibler (KL) divergence ([Kullback and Leibler, 1951](#)). Throughout, $q(\boldsymbol{\theta}; \boldsymbol{\zeta})$ denotes a parametric approximation to the posterior distribution of $\boldsymbol{\theta}$, where the approximate-distribution parameters $\boldsymbol{\zeta}$ belong to a space \mathcal{Z} .

If inference is required for a single dataset $\mathbf{y}_1, \dots, \mathbf{y}_n$ only, the parameters $\boldsymbol{\zeta}$ can be chosen to minimize the KL divergence between $p(\boldsymbol{\theta} \mid \mathbf{y}_1, \dots, \mathbf{y}_n)$ and $q(\boldsymbol{\theta}; \boldsymbol{\zeta})$:

$$\begin{aligned} \hat{\boldsymbol{\zeta}} &= \arg \min_{\boldsymbol{\zeta}} \text{KL}\{p(\boldsymbol{\theta} \mid \mathbf{y}_1, \dots, \mathbf{y}_n) \parallel q(\boldsymbol{\theta}; \boldsymbol{\zeta})\} \\ &= \arg \max_{\boldsymbol{\zeta}} \int_{\Theta} \log \{q(\boldsymbol{\theta}; \boldsymbol{\zeta})\} p(\boldsymbol{\theta} \mid \mathbf{y}_1, \dots, \mathbf{y}_n) d\boldsymbol{\theta}. \end{aligned} \quad (18)$$

However, solving this optimization problem is often computationally demanding even for a

single dataset. To circumvent this challenge and amortize our inference framework, one may construct a mapping $\hat{\zeta} : \mathcal{S} \rightarrow \mathcal{Z}$ that transforms data into the optimal parameters, which can be obtained by solving

$$\begin{aligned} \hat{\zeta}(\cdot) &= \arg \min_{\zeta(\cdot)} \mathbb{E}_{\mathbf{Y}_1, \dots, \mathbf{Y}_n} \text{KL} \{p(\boldsymbol{\theta} \mid \mathbf{Y}_1, \dots, \mathbf{Y}_n) \parallel q(\boldsymbol{\theta}; \zeta(\mathbf{Y}_1, \dots, \mathbf{Y}_n))\} \\ &= \arg \max_{\zeta(\cdot)} \int_{\mathcal{S}^n} \int_{\Theta} \log \{q(\boldsymbol{\theta}; \zeta(\mathbf{y}_1, \dots, \mathbf{y}_n))p(\mathbf{y}_1, \dots, \mathbf{y}_n \mid \boldsymbol{\theta})p(\boldsymbol{\theta})\} d\boldsymbol{\theta} d\mathbf{y}_1 \cdots d\mathbf{y}_n. \end{aligned} \quad (19)$$

This mapping can be modeled using a neural network $\hat{\zeta}_\gamma : \mathcal{S} \rightarrow \mathcal{Z}$ parameterized by γ , trained by minimizing a Monte Carlo approximation of the expected KL divergence in (19):

$$\hat{\gamma} = \arg \max_{\gamma} \sum_{k=1}^K \log q(\boldsymbol{\theta}^{(k)}; \hat{\zeta}_\gamma(\mathbf{y}_1^{(k)}, \dots, \mathbf{y}_n^{(k)})). \quad (20)$$

Once trained, the neural network $\hat{\zeta}_{\hat{\gamma}}(\cdot)$ can be used to estimate (18) given an observed dataset at almost no computational cost. The neural network $\hat{\zeta}_{\hat{\gamma}}(\cdot)$ and the corresponding approximate distribution $q(\cdot; \hat{\zeta})$ are collectively referred to as an NPE.

There are numerous choices for the approximate distribution $q(\cdot; \zeta)$. A simple option is a multivariate Gaussian distribution (e.g., [Chan et al., 2018](#)), where ζ comprises the mean vector and the non-zero entries of the lower Cholesky factor of the covariance matrix. More flexible alternatives include Gaussian mixtures (e.g., [Papamakarios and Murray, 2016](#)) and trans-Gaussian distributions (e.g., [Maceda et al., 2024](#)). However, the most widely used approach is to adopt normalizing flows for their ability to approximate essentially any arbitrary density functions (e.g., [Ardizzone et al., 2019a](#); [Kobyzev et al., 2020](#); [Radev et al., 2020](#); [Papamakarios et al., 2021](#)). A normalizing flow defines a flexible distribution by transforming a simple base distribution (e.g., standard Gaussian) via a sequence of invertible and differentiable mappings, chosen so that the resulting density remains tractable via the change-of-variables formula. This enables efficient density evaluation during training (e.g., when optimizing (20)) and efficient sampling at inference time. A particularly popular and expressive class is the so-called affine coupling flow (e.g., [Dinh et al., 2016](#); [Kingma and Dhariwal, 2018](#); [Ardizzone et al., 2019b](#)), which is a universal density approximator ([Teshima](#)

et al., 2020) and is the approximate distribution adopted in this work.

Finally, selecting an appropriate architecture, that is, the functional form of the neural network $\hat{\zeta}_\gamma(\cdot)$, is crucial and should reflect the structure of the data. Since the data structure remains unchanged whether constructing an NBE or NPE, the same architecture can be employed in both cases, with the only difference being the output space of the network. In our setting, we adopt the DeepSets architecture:

$$\hat{\zeta}_\gamma(\mathbf{y}_1, \dots, \mathbf{y}_n) = \phi \left\{ \frac{1}{n} \sum_{i=1}^n \psi(\mathbf{y}_i), \log(n) \right\}, \quad (21)$$

where ϕ and ψ are dense MLPs (with γ combining their parameters), and the output space of ϕ is the space \mathcal{Z} of approximation-distribution parameters.

4. Simulation study

To validate the estimators described in Section 3, we now conduct a simulation study with data generated from our proposed model (5). Section 4.1 first details the setting of our simulation study, and Section 4.2 discusses the results.

4.1. Setting

To assess our methods, we consider the bivariate case with the below model specifications:

- R follows the univariate eGPD in (4) with parameters $\boldsymbol{\theta}_R = (\kappa, \sigma, \xi)^\top \in (0, \infty)^3$;
- $\mathbf{L} = (V_1, 1 - V_1)^\top$ is defined in terms of the random variable V_1 assumed to follow the symmetric Beta(θ_L, θ_L) distribution, where $\theta_L > 0$ is a shape parameter controlling the strength of dependence in the lower tail. This ensures that $\|\mathbf{L}\|_1 = 1$ as required. Note that, with this specification, the moment condition $\mathbb{E}(L_j^{-\kappa}) < \infty$ is satisfied if and only if $\theta_L > \kappa$; in this case, the lower tail structure of \mathbf{Y} is determined by (9)–(10). When $\theta_L < \kappa$, it is instead determined by (11)–(12). We can further show that in our setting, \mathbf{L}^{-1} is multivariate regularly varying with index $\alpha_{\mathbf{L}^{-1}} = \theta_L$ and limit measure $\nu_{\mathbf{L}^{-1}}([\mathbf{0}, \mathbf{y}]^C) = \nu_{L_1^{-1}}((y_1, \infty)) + \nu_{L_2^{-1}}((y_2, \infty)) \propto (y_1^{-\theta_L} + y_2^{-\theta_L})$ being the sum of marginal limit measures, which corresponds to asymptotic independence of the

components L_1^{-1} and L_2^{-1} . To avoid this case and make sure the moment condition is always satisfied, one could also shift and rescale the Beta distribution of V_1 to the support $[\epsilon, 1 - \epsilon]$ for some small $\epsilon > 0$, but we do not investigate this possibility here;

- $\mathbf{U} = (U_1, 1 - U_1)^\top$ is defined in terms of the random variable U_1 assumed to follow the symmetric Beta(θ_U, θ_U) distribution, where $\theta_U > 0$ is a shape parameter controlling the strength of dependence in the upper tail. This ensures that $\|\mathbf{U}\|_1 = 1$ as required;
- $\omega(u)$, $u \in [0, 1]$, is a Beta(3, 3) cumulative distribution function, taking as input the argument $(u - \theta_\omega)/(1 - 2\theta_\omega)$, where $\theta_\omega \in (0, 0.5)$ is a parameter controlling the transition region between the lower and upper tails.

Under this model specification, the parameters of the model are $\boldsymbol{\theta} = (\kappa, \sigma, \xi, \theta_L, \theta_U, \theta_\omega)^\top$ in the space $\Theta = (0, \infty)^5 \times (0, 0.5)$. Figure 1 displays simulations from the model for various choices of parameter values for which the moment condition $\mathbb{E}(L_j^{-\kappa}) < \infty$ is satisfied. These plots illustrate the model’s flexibility, and its ability to separately control the lower and upper tail structures through the parameters κ, θ_L (lower tail) and ξ, θ_U (upper tail).

To infer the model parameters, we use the hybrid likelihood–moment estimators (using the covariances as in (14) to estimate θ_ω), as well as neural estimators. Specifically, we train an ensemble (Sainsbury-Dale et al., 2025b) of five NBEs (see Section 3.2.1) under the L^1 loss, $\ell(\boldsymbol{\theta}, \hat{\boldsymbol{\theta}}) = \|\boldsymbol{\theta} - \hat{\boldsymbol{\theta}}\|_1$, along with a single NPE (Section 3.2.2). The neural networks used in both (17) and (21) follow the DeepSets architecture, where the functions ϕ and ψ are MLPs with three hidden layers of width 128 and ReLU activation functions. Before passing data through the neural networks, we apply a variance-stabilizing transformation, $h(x) = \text{sign}(x) \log(1 + |x|) - 1$. For posterior inference with the NPE, we use a normalizing flow based on affine coupling blocks (e.g., Dinh et al., 2016; Kingma and Dhariwal, 2018; Ardizzone et al., 2019b), with default hyperparameters as documented in our chosen software. We train the neural networks by sampling $K = 10^5$ parameter vectors from the following marginal priors, chosen to be relatively vague: $\kappa \sim \text{Unif}(0.1, 10)$, $\sigma \sim \text{Unif}(0.1, 3)$, $\xi \sim \text{Unif}(0, 0.5)$, $\theta_L \sim \text{Unif}(0.1, 20)$, $\theta_U \sim \text{Unif}(0.1, 20)$, and $\theta_\omega \sim \text{Unif}(0, 0.5)$. We then generate K sample sizes from the discrete uniform distribution, $n \sim \text{Unif}\{1000, \dots, 4000\}$, and, conditionally on each parameter-vector and sample-size pair, we simulate a dataset from the model (5). For

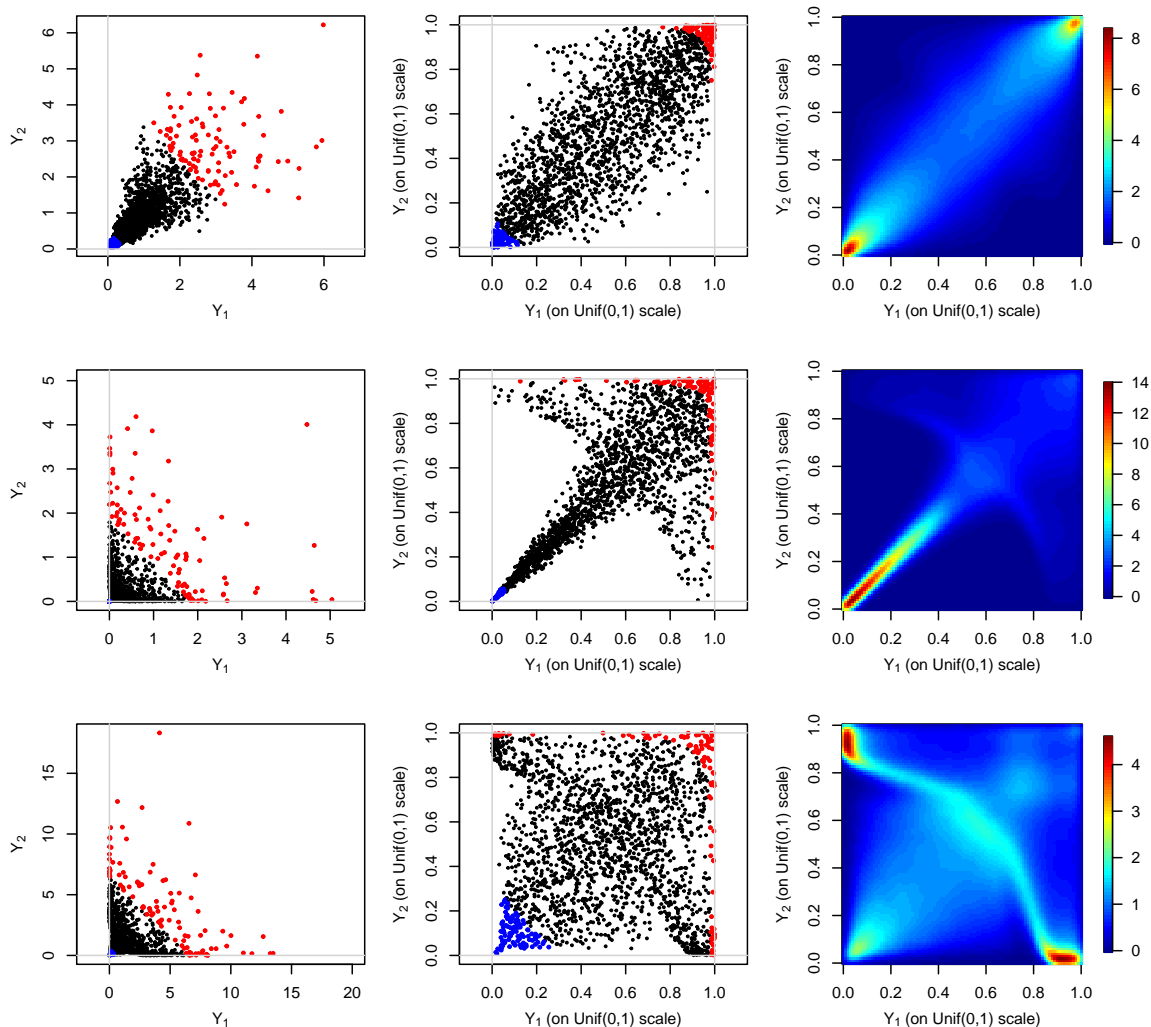


Figure 1: Sample of size $n = 2000$ from the multivariate eGPD model (5) with the parametric specification specified in Section 4.1, with $\theta = (\kappa, \sigma, \xi, \theta_L, \theta_U, \theta_\omega)^\top$ set to $(3, 1, 0.05, 10, 20, 0.25)^\top$ (top), $(0.3, 1, 0.05, 10, 0.5, 0.25)^\top$ (middle row), and $(3, 1, 0.2, 4, 0.5, 0.25)^\top$ (bottom), plotted on the original marginal scale (left), or rank-transformed to the Unif(0,1) scale (middle column) with a corresponding bivariate kernel density estimate (right). Red and blue points in the first two columns highlight “high extremes” (here, the top 5% of $\|\mathbf{Y}\|_1$ values) and “low extremes” (here, the lowest 5% of $\|\mathbf{Y}\|_1$ values).

the validation set used to monitor convergence during training, we generate $K/10$ parameter-data pairs in a similar manner. We cease training when the objective function in (15) or (20) has not decreased in ten consecutive epochs, where an epoch is defined to be one complete pass through the entire training dataset when doing stochastic gradient descent.

Our experiments are implemented using the package **NeuralEstimators** (Sainsbury-Dale, 2024), which is available in Julia and R. We use a workstation with an AMD Ryzen Threadripper Pro 5995WX CPU with 64 cores and 256 GB of RAM, and a NVIDIA RTX

A4500 GPU with 21 GB of RAM. All results presented in this section are reproducible via the code available at <https://github.com/alotaibin/multivariateEGPD>.

With these specifications, the total training time for the NBEs and NPE are 17.9 and 11.3 hours, respectively. While this can seem substantial, recall that these neural inference methods are amortized, meaning that the computational cost can be offset by applying the neural network repeatedly at the inference stage, almost instantaneously.

4.2. Results

To assess the estimators, we use a test set of 1000 parameter-data samples with a fixed sample size of $n = 4000$. Figure 2 presents recovery plots for the likelihood–moment-based estimator (top), the NBEs (middle), and the posterior medians obtained from the NPE (bottom). While all estimators generally yield sensible results, the likelihood–moment-based estimators exhibit higher overall variability compared to the neural approaches. The benefits of neural estimators are particularly evident for the more challenging parameters, namely, the weight function parameter θ_ω and the tail parameters θ_L and θ_U . Overall, both classes of neural estimators perform well in terms of statistical efficiency. In terms of computational efficiency, the neural methods offer substantial speedups once trained. For a single dataset with $n = 4000$ observations, inference using the NBEs takes 0.004 seconds, the NPE takes 0.007 seconds, whereas the likelihood–moment-based estimator requires 4.2 seconds.

To better evaluate the accuracy of the approximate posterior distributions obtained from the NPE, we employ several diagnostic tools commonly used in simulation-based inference. Figure 3 presents a suite of such diagnostic plots. The top row shows an empirical cumulative distribution function (ECDF) version of posterior-prior rank histograms, also known as simulation-based calibration (SBC) plots (Talts et al., 2018; Säilynoja et al., 2022; Modrák et al., 2025). If the posterior distributions are calibrated, the ECDF curves should lie within the confidence bands and closely follow the diagonal. This is indeed the case in our results, suggesting that the NPE posterior approximations are well-calibrated across the test set.

The second row of Figure 3 plots the posterior z -scores against posterior contractions (Schad et al., 2021). The posterior z -score is defined as the difference between the posterior mean and the true parameter value, divided by the posterior standard deviation. The poste-

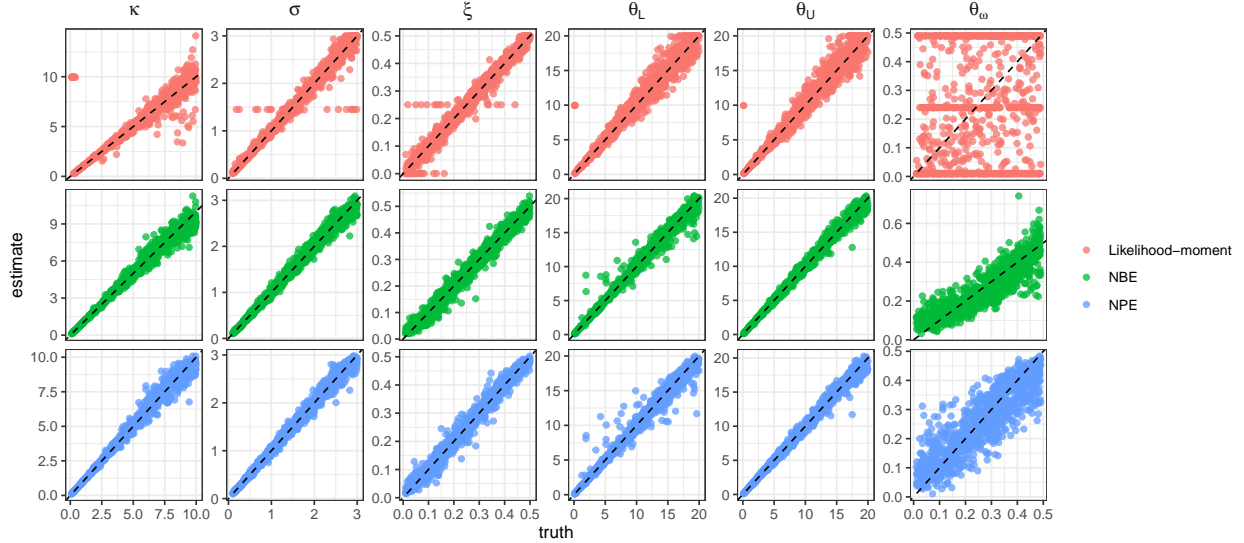


Figure 2: Recovery plots for the likelihood-moment-based estimator (top), NBEs (middle), and posterior medians obtained from the NPE (bottom), for the parameters κ , σ , ξ , θ_L , θ_U , and θ_ω (left to right), based on test data sampled from model (5) under the specification described in Section 4.1. Each plot displays parameter estimates against the true values used to generate the test data, with a fixed sample size of $n = 4000$ per dataset.

rior contraction is defined as $1 - \text{var}(\theta \mid \mathbf{Y})/\text{var}(\theta)$ for a given parameter θ , and reflects how much information has been gained from the data. In most cases, a well-calibrated posterior should lead to posterior z -scores that are centered around zero with unit variance, while posterior contraction values close to 1 indicate strong learning from the data. In our results, the posterior z -scores show no systematic bias for any parameter, and the posterior contractions are high for most parameters. However, for the more challenging parameter θ_ω , contractions are occasionally lower, reflecting inherent difficulty in estimating this component reliably.

The remaining rows of Figure 3 show the full approximate posterior distributions for each parameter across three test cases previously shown in Figure 1. Across all cases, the true parameter values (shown as vertical dashed lines) lie within the support of the approximate posterior distributions. Collectively, these diagnostics provide empirical support that the NPE approximates the true posterior well across the test datasets.

5. Analysis of three Dutch precipitation time series

Modeling low, moderate and extreme rainfall jointly across multiple locations is useful for regional flood-risk assessment and planning: severe floods can arise from single heavy storms

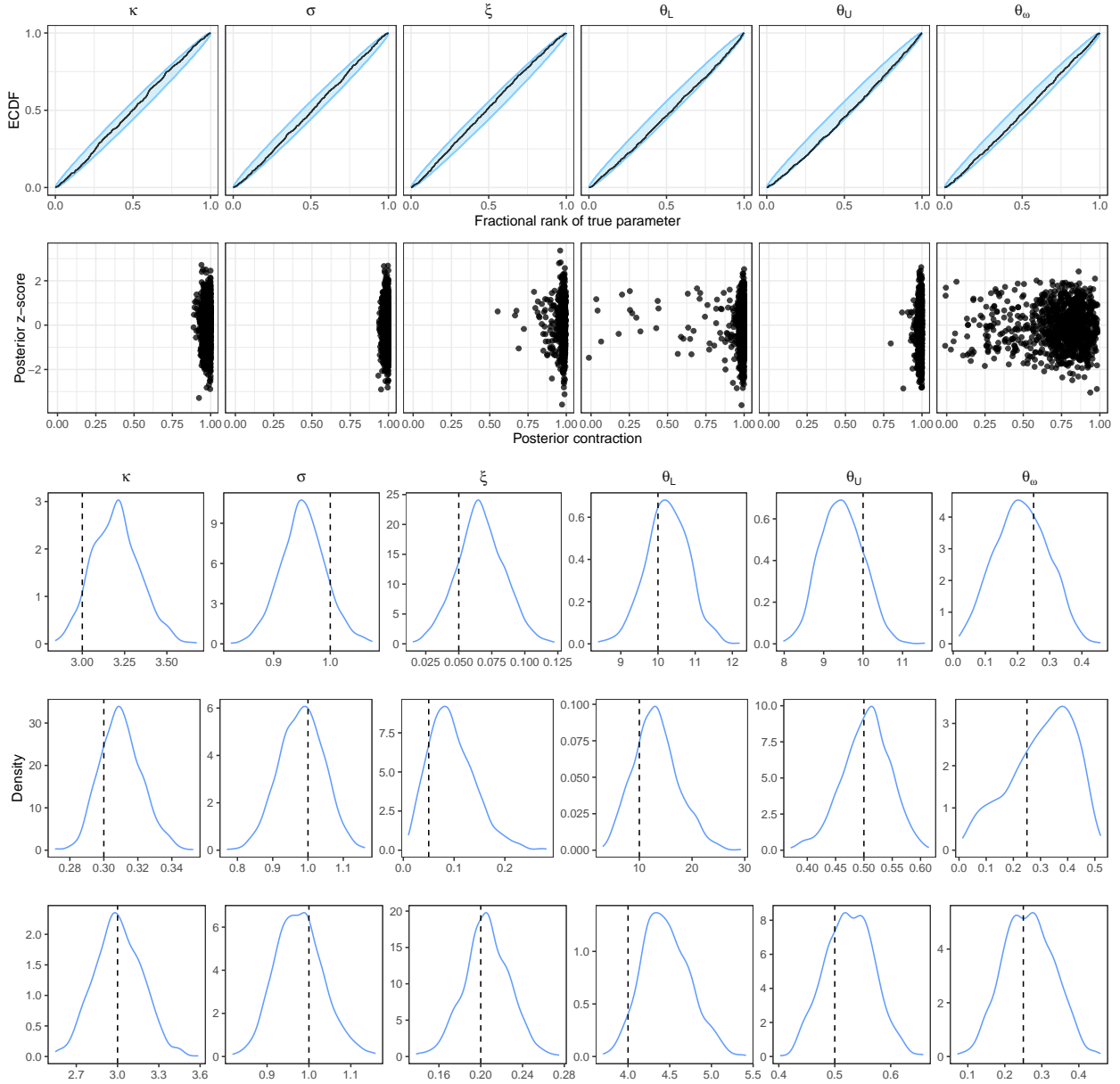


Figure 3: Diagnostic plots assessing the quality of the approximate posterior distributions obtained from the NPE. (Top row) ECDF versions of posterior-prior rank histogram plots, with shaded confidence bands. For well-calibrated posteriors, the curves should lie within the confidence bands. (Second row) Posterior z -scores against posterior contractions for each parameter. (Remaining rows) Approximate posterior distributions (blue curves) for each model parameter across three test cases (top to bottom), for three test cases with true parameter values (dashed black vertical lines) corresponding to those displayed in Figure 1.

or from accumulations of more moderate rainfall events. To illustrate our multivariate eGPD, we use daily precipitation totals (mm) from three North Brabant meteorological stations in the Netherlands: Ammerzoden, Giersbergen, and Zaltbommel (see Table 1) obtained from

Table 1: Station metadata: IDs, names, coordinates and elevations for the three North Brabant sites.

ID	Station	Latitude (°N)	Longitude (°E)	Elev. (m)
2357	Ammerzoden	51.75	5.2167	2
2417	Giersbergen	51.65	5.1500	6
2556	Zaltbommel	51.80	5.2667	2

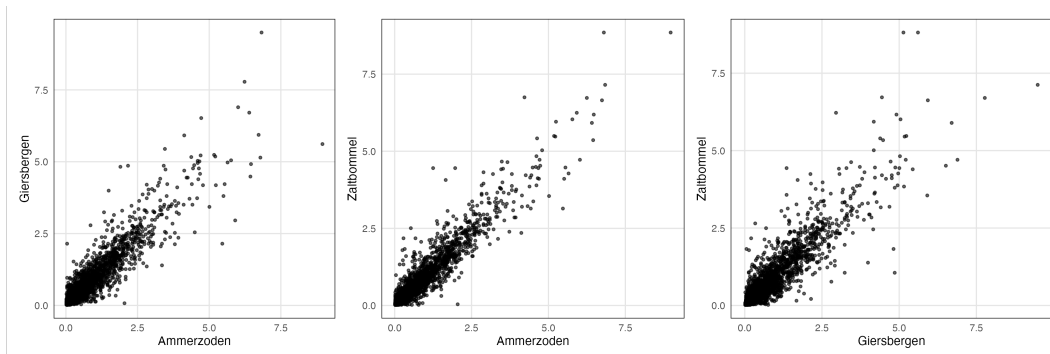


Figure 4: Pairwise scatterplots of fall–winter daily scaled precipitation for the three station pairs: Ammerzoden–Giersbergen (left), Ammerzoden–Zaltbommel (center) and Giersbergen–Zaltbommel (right).

the European Climate Assessment & Dataset (ECA&D; [Klein Tank et al., 2002](#)). Following [Bortot and Gaetan \(2024\)](#), we retain only the fall–winter months (October–February) over 1999–2024 and eliminate all zero-rain days, producing $n = 2\,138$, $2\,166$, and $2\,133$ positive observations at the three considered stations, respectively. Figure 4 shows pairwise scatterplots of the daily precipitation totals (mm) scaled by their empirical standard deviations for each station pair, highlighting the dependence across the full intensity range.

We fit the bivariate version of our eGPD (5) to each pair of stations using our trained NPE under the same settings given in Section 4. Table 2 reports the resulting point estimates and 95% credible intervals for κ , σ , ξ , θ_L , θ_U and θ_ω . Notably, the lower-tail parameter θ_L , and the upper-tail parameter θ_U are largest for the Ammerzoden–Zaltbommel pair, reflecting its stronger dependence at small and large rainfall amounts, while the upper-tail is moderately heavy (as reflected by ξ) across all three pairs, in line with typical extreme rainfall behavior.

Diagnostic plots for the Ammerzoden–Zaltbommel fit are shown in Figure 5; results for the other two pairs appear in [Appendix A](#). In the scaled scatterplot, observed points (red) and model simulations (blue) coincide closely across both the bulk and the tails, indicating that the dependence patterns are well captured. To assess the extremal dependence behavior,

Table 2: Neural posterior median estimates (bold) and 95% posterior credible intervals for the multivariate eGPD parameters at each station pair.

Parameter	Ammerzoden–Giersbergen	Ammerzoden–Zaltbommel	Giersbergen–Zaltbommel
κ	1.196 (1.097, 1.304)	1.116 (1.032, 1.215)	1.268 (1.161, 1.407)
σ	1.313 (1.157, 1.484)	1.381 (1.226, 1.553)	1.214 (1.068, 1.380)
ξ	0.216 (0.157, 0.281)	0.193 (0.136, 0.259)	0.242 (0.176, 0.307)
θ_L	3.955 (3.476, 4.439)	4.082 (3.488, 4.752)	3.593 (3.190, 4.048)
θ_U	18.335 (16.658, 20.336)	21.043 (19.358, 22.980)	14.999 (13.371, 16.881)
θ_ω	0.421 (0.263, 0.492)	0.237 (0.083, 0.401)	0.485 (0.417, 0.504)

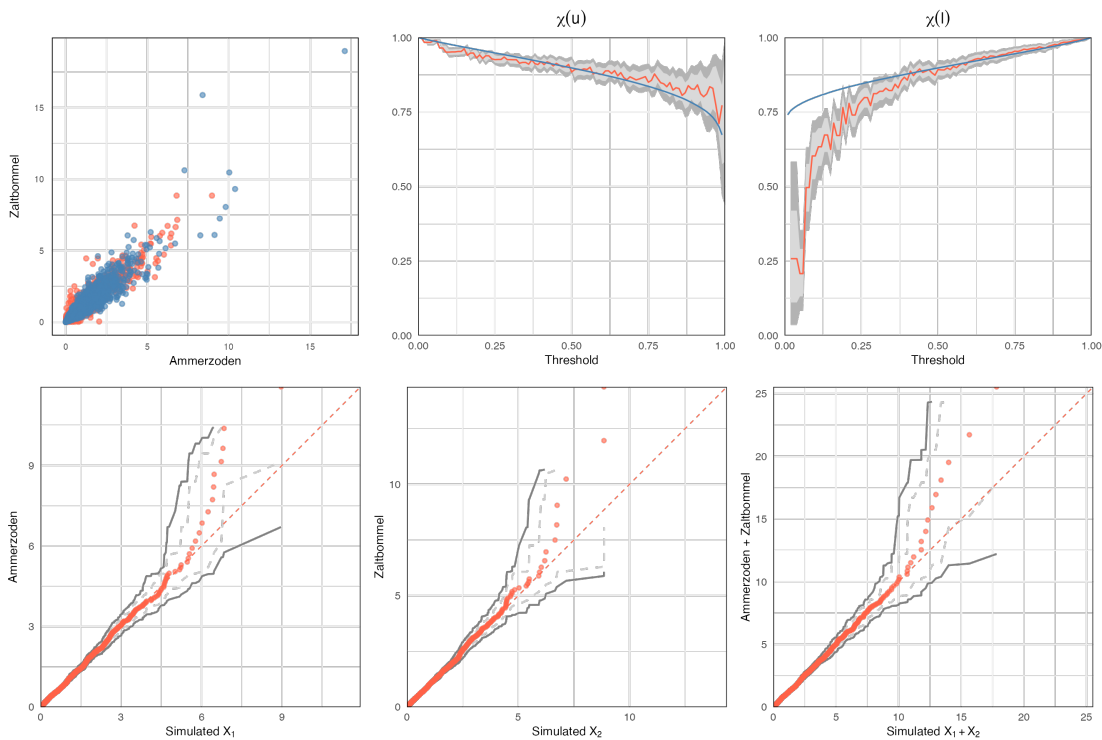


Figure 5: Diagnostics for the Ammerzoden–Zaltbommel fit. Top: Real (red) and simulated (blue) scatterplot based on the estimated parameters (left), and the χ -dependence measures for the upper (middle) and lower (right) tails, computed based on observed (red) and simulated (blue) data, with 95% bootstrap overall error bands (dark gray) and pointwise error bands (light grey). Bottom: QQ plots of observed versus simulated data for each margin (left and middle) and for the joint distribution summarized by the sum across stations (right). The 95% overall error (dark gray line), and the pointwise confidence bands (dashed light gray) were obtained by bootstrapping. Recall that the data have been rescaled by their empirical standard deviations.

that is, whether large rainfall amounts at separate stations tend to occur simultaneously, we plot the χ -measure (Coles et al., 1999) for the true (red) and the model-based (blue) joint upper-tail exceedances (and symmetrically for the joint lower-tail), together with the 95% overall error envelopes and pointwise bootstrap confidence bands. These curves show that

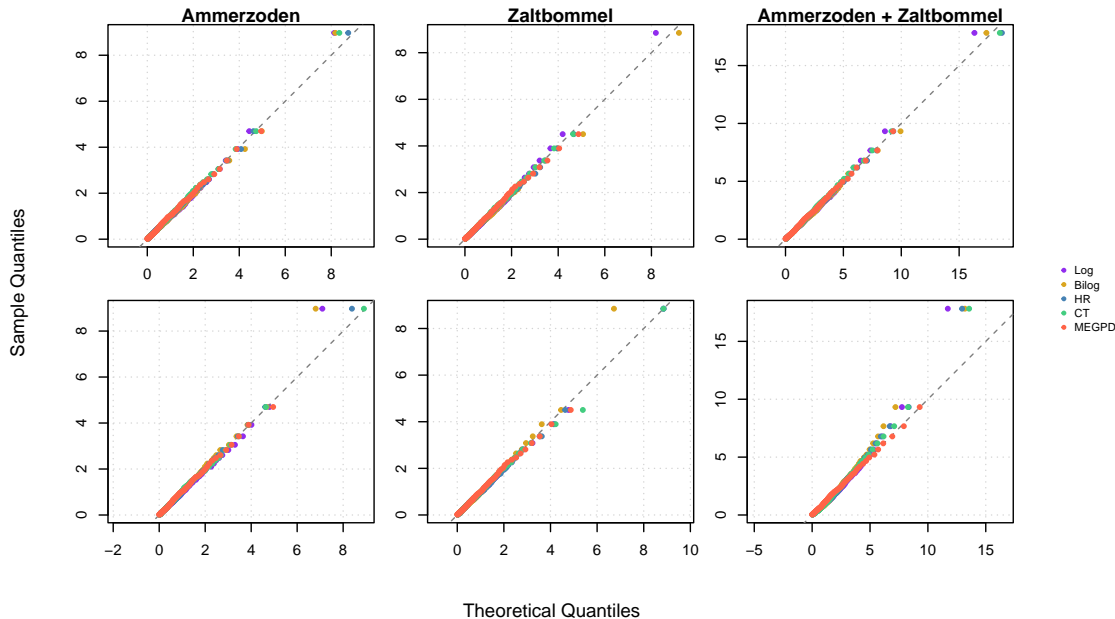


Figure 6: QQ-plots for marginal (left and middle) and joint (right; summarized by the sum across stations) distributions, comparing classical bivariate GP models fitted to data from the upper tail (top) or lower tail (bottom), versus our multivariate eGPD model fitted to the entire dataset, for the Ammerzoden–Zaltbommel pair. Thresholds are selected as 2.83 mm (Ammerzoden) and 2.81 mm (Zaltbommel) for the upper tail, and 0.082 mm (Ammerzoden) and 0.077 mm (Zaltbommel) for the lower tail (after rescaling by the empirical standard deviation). For readability, the QQ-plots are displayed after transforming data from each tail to a common exponential scale (so, for the lower tail, small values are to the right of each panel). Classical bivariate GP fits include the logistic (“Log”; purple), bilogistic (“Bilog”; yellow), Hüsler–Reiss (“HR”; blue), and Coles–Tawn (“CT”; green) models, along with our multivariate eGPD model (“MEGPD”; orange).

the model accurately reproduces the asymptotic dependence in the upper tails, while lower-tail estimates exhibit some lack-of-fit at small levels. We note that, similar to the issues pointed out by [Naveau et al. \(2016\)](#), there are very few distinct rainfall values below the 20% quantile (due to the limited precision of the measuring instrument), which reduces the information available for the lower tail and causes some model misspecification due to the discrete nature of the data; this likely explains the slightly larger bias observed in the lower-tail χ -measure at small levels. Nevertheless, quantile-quantile (QQ)-plots of the simulated versus observed marginal and joint distributions, together with 95% overall error envelopes and pointwise bootstrap confidence bands, demonstrate reliable fits and extrapolation to extreme quantiles. Overall, our proposed model thus provides satisfactory marginal and dependence fits from low to high quantiles.

Finally, to benchmark our modeling framework against classical extreme-value approaches, Figure 6 displays marginal and joint QQ-plots for the Ammerzoden–Zaltbommel pair where we overlay our multivariate eGPD fit (based on the entire dataset) with four standard bivariate generalized Pareto (GP) models—namely, logistic (“Log”; Gumbel, 1960), bilogistic (“Bilog”; Smith, 1990), Hüsler–Reiss (“HR”; Hüsler and Reiss, 1989) and Coles–Tawn (“CT”; Coles and Tawn, 1991)—fitted either to data from the upper tail (first row) or data from the lower tail (bottom row). Precisely, each classical extreme-value model is fitted separately to the lowest 10% of fall–winter rainfall totals (≤ 0.082 mm at Ammerzoden, ≤ 0.077 mm at Zaltbommel, after rescaling) and to the highest 5% of totals (≥ 2.83 mm at Ammerzoden, ≥ 2.81 mm at Zaltbommel, after rescaling). The joint and marginal fits (displayed after transforming the data to a common exponential scale, for readability) appear to capture joint high and low rainfall extremes effectively. The close agreement between the bivariate GP models and our multivariate eGPD suggests that our approach has the same capacity at representing the high and low rainfall data as the classical bivariate GP model, with the added advantage of modeling moderate rainfall effectively. In other words, our model provides an accurate description of the full range of the rainfall data in this example.

6. Conclusion

In this work, we analyze high and low extremes in a multivariate context, while completely bypassing the complex threshold selection step usually required in extreme-value analyses. We achieve this by extending the univariate extended generalized Pareto distribution widely used in environmental modeling. Our proposed modeling framework offers great flexibility, as practitioners can freely choose parametric distributions for the nonnegative random vectors \mathbf{L} and \mathbf{U} in (5) (on the simplex), which characterize dependence in the lower and upper tails. While parameter estimation is notoriously challenging with classical models for multivariate extremes, our model construction allows for straightforward and fast simulation, which enables simulation-based inference methods that avoid likelihood-function computations. In particular, our simulation experiments show that neural networks can efficiently approximate the entire posterior distribution of model parameters or point summaries thereof.

Despite its advantages, our modeling framework also has certain limitations. A first

limitation of our model is that the vectors \mathbf{L} and \mathbf{U} , while primarily controlling the dependence structure, also affect the marginal distributions. This may be particularly problematic when a permutation-asymmetric dependence structure must be specified, as choosing non-identically distributed components L_j and/or U_j would also (differently) impact the marginal scale of each variable Y_j . In our application, this was not a problem because we scaled the data by their empirical standard deviation and fitted a model with permutation-symmetric \mathbf{L} and \mathbf{U} . If this is a problem in future applications, it would be easy to mitigate it by extending the multivariate eGPD model in (5) to allow for different marginal scale parameters. This can be achieved by defining the random vector $\mathbf{Z} = (Z_1, \dots, Z_d)^\top$ as $\mathbf{Z} = \boldsymbol{\sigma}\mathbf{Y}$, where \mathbf{Y} is defined as in (5) but setting $\sigma = 1$, and where $\boldsymbol{\sigma} = (\sigma_1, \dots, \sigma_d)^\top$ with $\sigma_j > 0$, $j = 1, \dots, d$, comprises component-specific scale parameters. In case the margins of \mathbf{L} or \mathbf{U} are not identical, this discrepancy will be absorbed by the scale parameters σ_j .

Another related limitation is that, even with the above modification, all components Z_j of \mathbf{Z} (or Y_j in (5)) of our multivariate eGPD model share the same lower tail shape parameter $\kappa > 0$ and upper tail shape parameter $\xi > 0$. While one might expect natural processes observed at different close-by locations to have similar tail behaviors in general, empirical evidence shows that they may vary over large or complex geographical domains. If that is an issue, another model extension allowing for component-specific scale and shape parameters can be obtained by replacing the random variable R in (5) with a random vector $\mathbf{R} = (R_1, \dots, R_d)^\top$ where $R_j = F_{R_j}^{-1}(U)$ and F_{R_j} is the univariate eGPD cumulative distribution function with parameters $\kappa_j, \sigma_j, \xi_j > 0$ and $U \sim \text{Unif}(0, 1)$ a uniform random variable. In this way, all components of \mathbf{R} are comonotonic (i.e., perfectly positively dependent) as in the original model, but they have their own specific marginal eGPD parameters. The precise theoretical study of the joint lower/upper tails in this framework is left for future research.

A final limitation of our proposed model is that it does not cover the case of asymptotic independence, which is often found as a plausible assumption with environmental data (Huser and Wadsworth, 2022; Huser et al., 2025). Further research is needed in this direction to develop more flexible tail models (but see, e.g., Gong and Huser, 2022; André et al., 2025).

We conclude by noting that no unique solution exists to extend the univariate eGPD to the multivariate context, and other options should thus be explored. For example, the

ongoing work of [Gaetan and Naveau \(2025\)](#) proposes a different type of multivariate eGPD based on a logistic-heteroscedastic model. Their model is designed so that the radial and angular components remain dependent at non-extreme levels. Another important difference between our current work and that of [Gaetan and Naveau \(2025\)](#) is how inference is performed. While our approach relies on an additive structure with dynamic weighting (recall (5)), which makes the likelihood function intractable, the heteroscedastic model of [Gaetan and Naveau \(2025\)](#) is amenable to likelihood-based inference when using a Gaussian vector in its construction. Overall, although both approaches stem from the same univariate eGPD seed, they lead to different multivariate models, each with their pros and cons.

Acknowledgments

Noura Alotaibi, Matthew Sainsbury-Dale, and Raphaël Huser were supported by King Abdullah University of Science and Technology (KAUST) under Award No. RFS-OFP2023-5550. Part of Philippe Naveau’s research work was supported by the French Agence Nationale de la Recherche: EXSTA, the PEPR TRACCS (PC4 EXTENDING, ANR-22-EXTR-0005), the PEPR IRIMONT (France 2030 ANR-22-EXIR-0003) SHARE PEPR Maths-Vives (ANR-24-EXMA-0008) and from the Geolearning research chair, a joint initiative of Mines Paris and the French National Institute for Agricultural Research (INRAE).

References

- Alouini, S., Belzile, L.R., Davison, A., 2026. Choosing the threshold in extreme value analysis. *Brazilian Journal of Probability and Statistics* To appear.
- André, L., Wadsworth, J.L., Huser, R., 2025. Neural Bayes inference for complex bivariate extremal dependence models. *ArXiv preprint arXiv:2503.23156*.
- André, L.M., Tawn, J.A., 2025. Gaussian mixture copulas for flexible dependence modelling in the body and tails of joint distributions. *ArXiv preprint arXiv:2503.06255*.
- André, L., Wadsworth, J., O’Hagan, A., 2024. Joint modelling of the body and tail of bivariate data. *Computational Statistics & Data Analysis* 189, 107841.
- Ardizzone, L., Kruse, J., Rother, C., Köthe, U., 2019a. Analyzing inverse problems with invertible neural networks, in: *Proceedings of the 7th International Conference on Learning Representations (ICLR 2019)*.
- Ardizzone, L., Lüth, C., Kruse, J., Rother, C., Köthe, U., 2019b. Guided image generation with conditional invertible neural networks. *ArXiv preprint arXiv:1907.02392*.
- Bacro, J.N., Gaetan, C., Opitz, T., Toulemonde, G., 2024. Multivariate peaks-over-threshold with latent variable representations of generalized Pareto vectors. *Extremes* 28, 273–300.

- Beirlant, J., Goegebeur, Y., Teugels, J., Segers, J., 2004. *Statistics of Extremes*. John Wiley & Sons Ltd., Chichester.
- Bortot, P., Gaetan, C., 2024. A model for space-time threshold exceedances with an application to extreme rainfall. *Statistical Modelling* 24, 169–193.
- Breiman, L., 1965. On some limit theorems similar to the arc-sin law. *Theory of Probability & Its Applications* 10, 323–331.
- Brunner, M.I., Papalexiou, S., Clark, M.P., Gilleland, E., 2020. How probable is widespread flooding in the United States? *Water Resources Research* 56, e2020WR028096.
- Carreau, J., Bengio, Y., 2008. A hybrid Pareto model for asymmetric fat-tailed data: the univariate case. *Extremes* 12, 53–76.
- Carreau, J., Bengio, Y., 2009. A hybrid Pareto mixture for conditional asymmetric fat-tailed distributions. *IEEE Transactions on Neural Networks* 20, 1087–1101.
- de Carvalho, M., Huser, R., Naveau, P., Reich, B., 2025. *Handbook on Statistics of Extremes*. Chapman & Hall / CRC.
- Casella, G., Berger, R., 2001. *Statistical Inference*. Second ed., Duxbury, Belmont, CA.
- Chan, J., Perrone, V., Spence, J., *et al.*, 2018. A likelihood-free inference framework for population genetic data using exchangeable neural networks, in: Bengio, S., Wallach, H., Larochelle, H., Grauman, K., Cesa-Bianchi, N., Garnett, R. (Eds.), *Advances in Neural Information Processing Systems*, pp. 8594–8605.
- Cisneros, D., Richards, J., Dahal, A., Lombardo, L., Huser, R., 2024. Deep graphical regression for jointly moderate and extreme Australian wildfires. *Spatial Statistics* 59, 100811.
- Coles, S., 2001. *An Introduction to Statistical Modeling of Extreme Values*. Springer, New York.
- Coles, S., Heffernan, J., Tawn, J., 1999. Dependence measures for extreme value analyses. *Extremes* 2, 339–365.
- Coles, S.G., Tawn, J.A., 1991. Modelling extreme multivariate events. *Journal of the Royal Statistical Society: Series B (Statistical Methodology)* 53, 377–392.
- Coloma, N., Kleiber, W., 2025. Fast likelihood-free parameter estimation for Lévy processes. ArXiv preprint arXiv.2501.01639.
- Davison, A.C., Huser, R., 2015. Statistics of Extremes. *Annual Review of Statistics and its Application* 2, 203–235.
- Davison, A.C., Smith, R.L., 1990. Models for exceedances over high thresholds (with discussion). *Journal of the Royal Statistical Society: Series B (Statistical Methodology)* 52, 393–442.
- Dinh, L., Sohl-Dickstein, J., Bengio, S., 2016. Density estimation using Real NVP, in: *Proceedings of the 4th International Conference on Learning Representations (ICLR 2016)*.
- Embrechts, P., Klüppelberg, C., Mikosch, T., 2013. *Modelling Extremal Events: for Insurance and Finance*. volume 33. Springer Berlin Heidelberg.
- Engelke, S., Opitz, T., Wadsworth, J., 2019. Extremal dependence of random scale constructions. *Extremes* 22, 623–666.

- Evin, G., Favre, A.C., Hingray, B., 2018. Stochastic generation of multi-site daily precipitation focusing on extreme events. *Hydrology and Earth System Sciences* 22, 655–672.
- Fischer, E.M., Bador, M., Huser, R., Kendon, E.J., Robinson, A., Sippel, S., 2025. Record-breaking extremes in a warming climate. *Nature Reviews Earth & Environment* 6, 456–470.
- de Fondeville, R., Davison, A.C., 2018. High-dimensional peaks-over-threshold inference. *Biometrika* 105, 575–592.
- Fougères, A.L., Mercadier, C., 2012. Risk measures and multivariate extensions of Breiman’s theorem. *Journal of Applied Probability* 49, 364–384.
- Frigessi, A., Haug, O., Rue, H., 2002. A dynamic mixture model for unsupervised tail estimation without threshold selection. *Extremes* 5, 219–235.
- Gaetan, C., Naveau, P., 2025. Multivariate distributional modeling of low, moderate, and large intensities without threshold selection steps. In preparation.
- Gamet, P., Jalbert, J., 2022. A flexible extended generalized Pareto distribution for tail estimation. *Environmetrics* 33, e2744.
- Gong, Y., Huser, R., 2022. Asymmetric tail dependence modeling, with application to cryptocurrency market data. *The Annals of Applied Statistics* 16, 1822–1847.
- Gumbel, E.J., 1960. Distributions des valeurs extremes en plusieurs dimensions. *Annales de l’ISUP* 9, 171–173.
- de Haan, L., Ferreira, A., 2006. *Extreme Value Theory: An Introduction*. Springer-Verlag, New York.
- Haruna, A., Blanchet, J., Favre, A.C., 2023. Modeling intensity-duration-frequency curves for the whole range of non-zero precipitation: a comparison of models. *Water Resources Research* 59, e2022WR033362.
- Haruna, A., Blanchet, J., Favre, A.C., 2024. Estimation of intensity-duration-area-frequency relationships based on the full range of non-zero precipitation from radar-reanalysis data. *Water Resources Research* 60, e2023WR035902.
- Hazra, A., Huser, R., Bolin, D., 2025. Efficient modeling of spatial extremes over large geographical domains. *Journal of Computational and Graphical Statistics* 34, 795–811.
- Hornik, K., Stinchcombe, M., White, H., 1989. Multilayer feedforward networks are universal approximators. *Neural Networks* 2, 359–366.
- Huser, R., Opitz, T., Thibaud, E., 2017. Bridging asymptotic independence and dependence in spatial extremes using Gaussian scale mixtures. *Spatial Statistics* 21, 166–186.
- Huser, R., Opitz, T., Wadsworth, J.L., 2025. Modeling of spatial extremes in environmental data science: Time to move away from max-stable processes. *Environmental Data Science* 4, 1–16.
- Huser, R., Wadsworth, J.L., 2022. Advances in statistical modeling of spatial extremes. *Wiley Interdisciplinary Reviews: Computational Statistics* 14, e1537.
- Hüsler, J., Reiss, R.D., 1989. Maxima of normal random vectors: between independence and complete dependence. *Statistics & Probability Letters* 7, 283–286.
- IPCC, 2023. *Climate Change 2023: Synthesis Report*, in: Core Writing Team, H.L., Romero, J. (Eds.), Contribution of Working Groups I, II, and III to the Sixth Assessment Report of the Intergovernmental Panel on Climate Change. IPCC, Geneva, Switzerland, pp. 35–115.

- Kakampakou, L., Simpson, E.S., Wadsworth, J.L., 2024. Spatial extremal modelling: A case study on the interplay between margins and dependence. *Stat* 13, e70021.
- Kingma, D.P., Dhariwal, P., 2018. Glow: Generative flow with invertible 1x1 convolutions, in: Bengio, S., Wallach, H., Larochelle, H., Grauman, K., Cesa-Bianchi, N., Garnett, R. (Eds.), *Advances in Neural Information Processing Systems*, Curran Associates, Inc.. pp. 10215–10224.
- Klein Tank, A.M.G., Wijngaard, J.B., Können, G.P., *et al.*, 2002. Daily dataset of 20th-century surface air temperature and precipitation series for the European Climate Assessment. *International Journal of Climatology* 22, 1441–1453.
- Kobyzev, I., Prince, S.J., Brubaker, M.A., 2020. Normalizing flows: An introduction and review of current methods. *IEEE Transactions on Pattern Analysis and Machine Intelligence* 43, 3964–3979.
- Krupskii, P., Huser, R., 2022. Modeling spatial tail dependence with Cauchy convolution processes. *Electronic Journal of Statistics* 16, 6135–6174.
- Kulik, R., Soulier, P., 2020. *Heavy-Tailed Time Series*. Springer, New York.
- Kullback, S., Leibler, R.A., 1951. On information and sufficiency. *Annals of Mathematical Statistics* 22, 79–86.
- Le Gall, P., Favre, A.C., Naveau, P., Prieur, C., 2022. Improved regional frequency analysis of rainfall data. *Weather and Climate Extremes* 36, 100456.
- Lenzi, A., Bessac, J., Rudi, J., Stein, M.L., 2023. Neural networks for parameter estimation in intractable models. *Computational Statistics and Data Analysis* 185, 107762.
- Maceda, E., Hector, E.C., Lenzi, A., Reich, B.J., 2024. A variational neural Bayes framework for inference on intractable posterior distributions. *ArXiv preprint arXiv:2404.10899*.
- Mackay, E., Jonathan, P., 2024. Modelling multivariate extremes through angular-radial decomposition of the density function. *ArXiv preprint arXiv:2310.12711*.
- McFadden, D., 1989. A method of simulated moments for estimation of discrete response models without numerical integration. *Econometrica* 57, 995–1026.
- Merz, B., Blöschl, G., Vorogushyn, S., Dottori, F., Aerts, J.C.J.H., Bates, P., Bertola, M., Kemter, M., Kreibich, H., Lall, U., Macdonald, E., 2021. Causes, impacts and patterns of disastrous river floods. *Nature Reviews Earth & Environment* 2, 592–609.
- Modrák, M., Moon, A.H., Kim, S., Bürkner, P., Huurre, N., Faltejsková, K., Gelman, A., Vehtari, A., 2025. Simulation-based calibration checking for Bayesian computation: The choice of test quantities shapes sensitivity. *Bayesian Analysis* 20, 461–488.
- Morris, S.A., Reich, B.J., Thibaud, E., Cooley, D., 2017. A space-time skew-t model for threshold exceedances. *Biometrics* 73, 749–758.
- Murphy-Barltrop, C.J.R., Mackay, E., Jonathan, P., 2024. Inference for bivariate extremes via a semi-parametric angular-radial model. *Extremes*, 1–30.
- Naveau, P., 2025. Jointly modeling the bulk and tails, in: de Carvalho, M., Huser, R., Naveau, P., Reich, B. (Eds.), *Handbook on Statistics of Extremes*. CRC Press. chapter 5.
- Naveau, P., Huser, R., Ribereau, P., Hannart, A., 2016. Modeling jointly low, moderate and heavy rainfall intensities without a threshold selection. *Water Resources Research* 52, 2753–2769.

- Papamakarios, G., Murray, I., 2016. Fast ϵ -free inference of simulation models with Bayesian conditional density estimation, in: Lee, D., Sugiyama, M., Luxburg, U., Guyon, I., Garnett, R. (Eds.), *Advances in Neural Information Processing Systems*, Curran Associates, Inc., Red Hook, NY. pp. 1028–1036.
- Papamakarios, G., Nalisnick, E., Rezende, D.J., Lakshminarayanan, S.M.B., 2021. Normalizing flows for probabilistic modeling and inference. *Journal of Machine Learning Research* 22, 1–64.
- Papastathopoulos, I., Tawn, J.A., 2013. Extended generalised Pareto models for tail estimation. *Journal of Statistical Planning and Inference* 143, 131–143.
- Radev, S.T., Mertens, U.K., Voss, A., Ardizzone, L., Köthe, U., 2020. BayesFlow: Learning complex stochastic models with invertible neural networks. *IEEE Transactions on Neural Networks and Learning Systems* 33, 1452–1466.
- Rentschler, J., Salhab, M., Jafino, B.A., 2022. Flood exposure and poverty in 188 countries. *Nature Communications* 13, 3527.
- Resnick, S.I., 1987. *Extreme Values, Regular Variation and Point Processes*. Springer-Verlag New York.
- Resnick, S.I., Stărică, C., 1997. Smoothing the Hill estimator. *Advances in Applied Probability* 29, 271–293.
- Richards, J., Sainsbury-Dale, M., Zammit-Mangion, A., Huser, R., 2025. Neural Bayes estimators for censored inference with peaks-over-threshold models. *Journal of Machine Learning Research* 25, 1–49.
- Rootzén, H., Segers, J., Wadsworth, J.L., 2018. Multivariate peaks over thresholds models. *Extremes* 21, 115–145.
- Rödder, A., Hentschel, M., Engelke, S., 2025. Theoretical guarantees for neural estimators in parametric statistics. *ArXiv:2506.18508*.
- Sainsbury-Dale, M., 2024. *NeuralEstimators: Likelihood-Free Parameter Estimation using Neural Networks*. R package version 0.1.2, <https://CRAN.R-project.org/package=NeuralEstimators>.
- Sainsbury-Dale, M., Richards, J., Zammit-Mangion, A., Huser, R., 2025a. Neural Bayes estimators for irregular spatial data using graph neural networks. *Journal of Computational and Graphical Statistics* 34, 1153–1168.
- Sainsbury-Dale, M., Zammit-Mangion, A., Cressie, N., Huser, R., 2025b. Neural parameter estimation with incomplete data. *ArXiv preprint arXiv.2501.04330*.
- Sainsbury-Dale, M., Zammit-Mangion, A., Huser, R., 2024. Likelihood-free parameter estimation with neural Bayes estimators. *The American Statistician* 78, 1–14.
- Scarrott, C., MacDonald, A., 2012. A review of extreme value threshold estimation and uncertainty quantification. *REVSTAT* 10, 33–60.
- Schad, D.J., Betancourt, M., Vasishth, S., 2021. Toward a principled Bayesian workflow in cognitive science. *Psychological Methods* 26, 103.
- Shi, M., Zhang, L., Risser, M.D., Shaby, B.A., 2024. Spatial scale-aware tail dependence modeling for high-dimensional spatial extremes. *ArXiv preprint arXiv:2412.07957*.
- Smith, R.L., 1990. Extreme value theory. *Handbook of Applicable Mathematics* 7, 18.

- Stein, M.L., 2021a. A parametric model for distributions with flexible behavior in both tails. *Environmetrics* 32, e2658.
- Stein, M.L., 2021b. Parametric models for distributions when interest is in extremes with an application to daily temperature. *Extremes* 24, 293–323.
- Swiss Re, 2019. Natural catastrophes and man-made disasters in 2018: “secondary” perils on the frontline. (Tech. Rep. No. 2).
- Säilynoja, T., Bürkner, P., Vehtari, A., 2022. Graphical test for discrete uniformity and its applications in goodness-of-fit evaluation and multiple sample comparison. *Statistics and Computing* 32.
- Talts, S., Betancourt, M., Simpson, D., Vehtari, A., Gelman, A., 2018. Validating Bayesian inference algorithms with simulation-based calibration. ArXiv preprint arXiv:1804.06788.
- Tencaliec, P., Favre, A.C., Naveau, P., Prieur, C., Nicolet, G., 2020. Flexible semiparametric generalized Pareto modeling of the entire range of rainfall amount. *Environmetrics* 31, e2582.
- Teshima, T., Ishikawa, I., Tojo, K., *et al.*, 2020. Coupling-based invertible neural networks are universal diffeomorphism approximators, in: Larochelle, H., Ranzato, M., Hadsell, R., Balcan, M., Lin, H. (Eds.), *Advances in Neural Information Processing Systems*, pp. 3362–3373.
- Vicente-Serrano, S.M., Quiring, S.M., Peña-Gallardo, M., Yuan, S., Domínguez-Castro, F., 2020. A review of environmental droughts: Increased risk under global warming? *Earth-Science Reviews* 201, 102953.
- Vrac, M., Naveau, P., Drobinsky, P., 2007. Modeling pairwise rainfall intensities. *Nonlinear Processes in Geophysics* 14, 789–797.
- Wadsworth, J., Tawn, J., Davison, A., Elton, D., 2017. Modelling across extremal dependence classes. *Journal of the Royal Statistical Society Series B: Statistical Methodology* 79, 149–175.
- Wadsworth, J.L., Tawn, J.A., 2022. Higher-dimensional spatial extremes via single-site conditioning. *Spatial Statistics* 51, 100677.
- Yadav, R., Huser, R., Opitz, T., 2021. Spatial hierarchical modeling of threshold exceedances using rate mixtures. *Environmetrics* 32, e2662.
- Yadav, R., Huser, R., Opitz, T., 2022. A flexible Bayesian hierarchical modeling framework for spatially dependent peaks-over-threshold data. *Spatial Statistics* 51, 100672.
- Yadav, R., Huser, R., Opitz, T., Lombardo, L., 2023. Joint modelling of landslide counts and sizes using spatial marked point processes with sub-asymptotic mark distributions. *Journal of the Royal Statistical Society Series C: Applied Statistics* 72, 1139–1161.
- Yadav, R., Lombardo, L., Huser, R., 2025. Statistics of extremes for landslides and earthquakes, in: M. de Carvalho, R. Huser, P.N., Reich, B. (Eds.), *Handbook on Statistics of Extremes*. CRC Press. chapter 27.
- Zaheer, M., Kottur, S., Ravanbakhsh, S., *et al.*, 2017. Deep sets, in: Guyon, I., Luxburg, U.V., Bengio, S., Wallach, H., Fergus, R., Vishwanathan, S., Garnett, R. (Eds.), *Proceedings of the 30th Conference on Neural Information Processing Systems*, pp. 3392–3402.
- Zammit-Mangion, A., Sainsbury-Dale, M., Huser, R., 2025. Neural methods for amortized inference. *Annual Reviews of Statistics and Its Application* 12, 311–335.

Zhang, L., Rohrbeck, C., Opitz, T., 2025. Subasymptotic models for spatial extremes, in: M. de Carvalho, R. Huser, P.N., Reich, B. (Eds.), Handbook on Statistics of Extremes. CRC Press. chapter 17.

Appendix A. Additional diagnostic plots for the other station pairs

Ammerzoden–Giersbergen

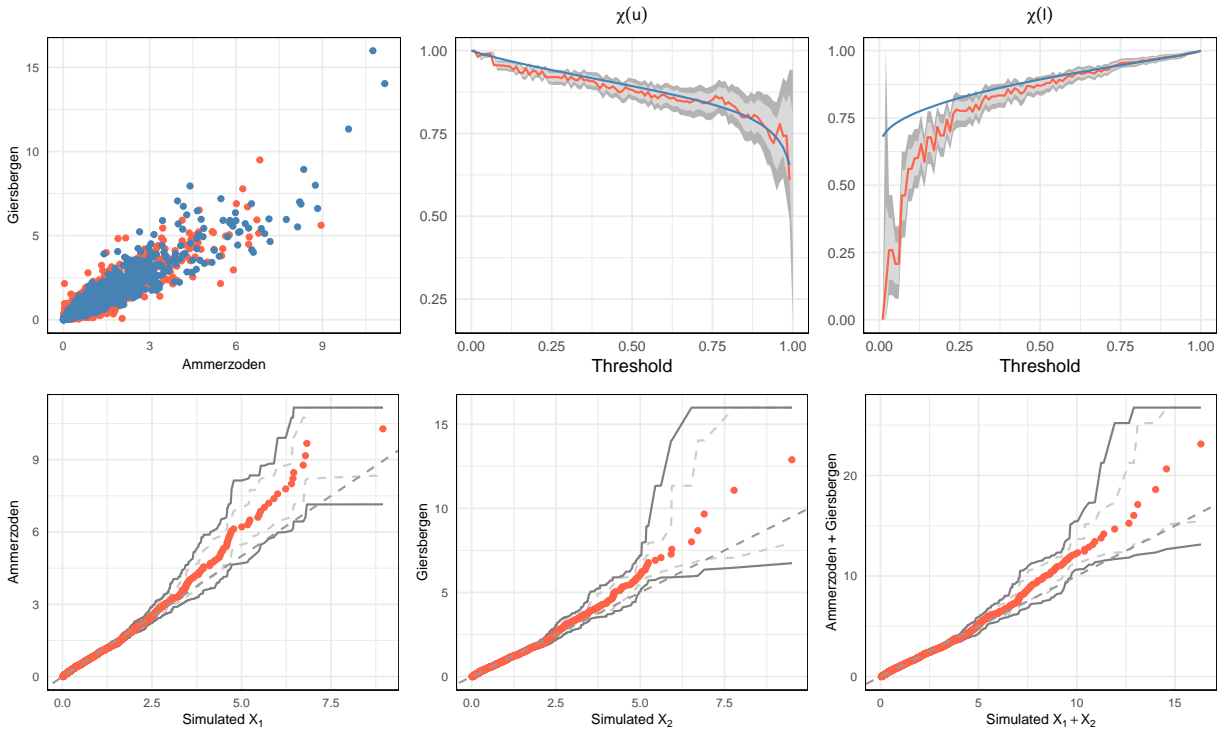


Figure A.7: Diagnostics for the Ammerzoden–Giersbergen fit. Top: Real (red) and simulated (blue) scatterplot based on the estimated parameters (left), and the χ -dependence measures for the upper (middle) and lower (right) tails, computed from observed (red) and simulated (blue) data, with 95% bootstrap overall error bands (dark gray) and pointwise error bands (light gray). Bottom: QQ-plots of observed versus simulated data for each margin (left and middle) and for the joint distribution summarized by the sum across stations (right). The 95% overall error (dark gray line) and the pointwise confidence bands (dashed light gray) were obtained by bootstrapping. Recall that the data have been rescaled by their empirical standard deviations.

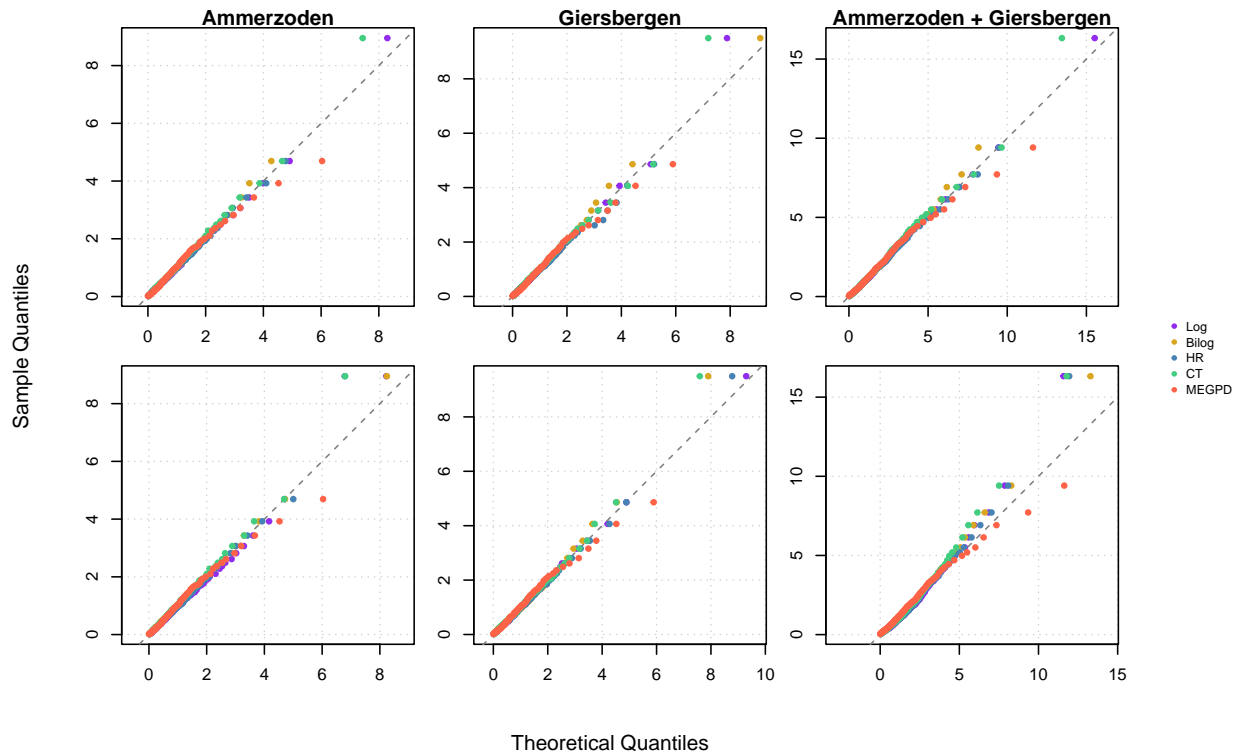


Figure A.8: QQ-plots for marginal (left and middle) and joint (right; summarized by the sum across stations) distributions, comparing classical bivariate GP models fitted to data from the upper tail (top) or lower tail (bottom), versus our multivariate eGPD model fitted to the entire dataset, for the Ammerzoden–Giersbergen pair. Thresholds are selected as 2.82 mm (Ammerzoden) and 2.81 mm (Giersbergen) for the upper tail, and 0.082 mm (Ammerzoden) and 0.094 mm (Giersbergen) for the lower tail (after rescaling by the empirical standard deviation). For readability, the QQ-plots are displayed after transforming data from each tail to a common exponential scale (so, for the lower tail, small values are to the right of each panel). Classical bivariate GP fits include the logistic (“Log”), bilogistic (“Bilog”), Hüsler–Reiss (“HR”), and Coles–Tawn (“CT”) models, along with our multivariate eGPD model (“MEGPD”).

Giersbergen–Zaltbommel

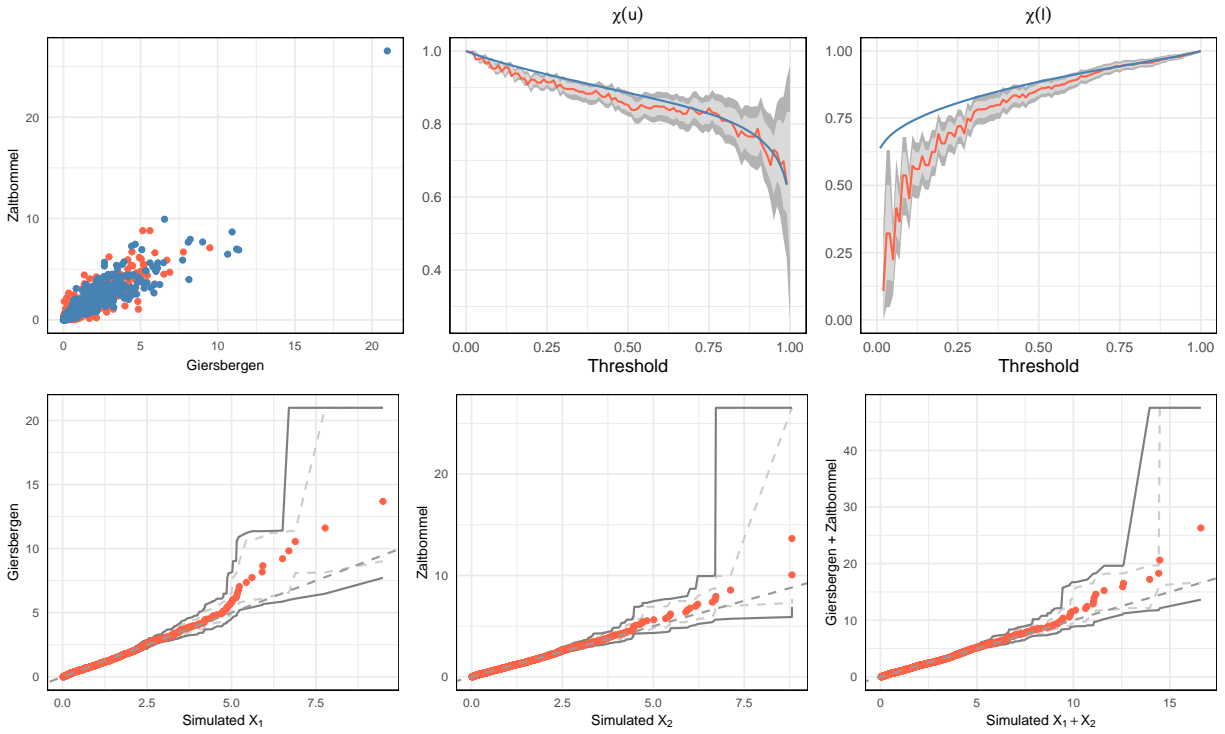


Figure A.9: Diagnostics for the Giersbergen–Zaltbommel fit. Top: Real (red) and simulated (blue) scatterplot based on the estimated parameters (left), and the χ -dependence measures for the upper (middle) and lower (right) tails, computed from observed (red) and simulated (blue) data, with 95% bootstrap overall error bands (dark gray) and pointwise error bands (light grey). Bottom: QQ-plots of observed versus simulated data for each margin (left and middle) and for the joint distribution summarized by the sum across stations (right). The 95% overall error (dark gray line) and the pointwise confidence bands (dashed light gray) were obtained by bootstrapping. Recall that the data have been rescaled by their empirical standard deviations.

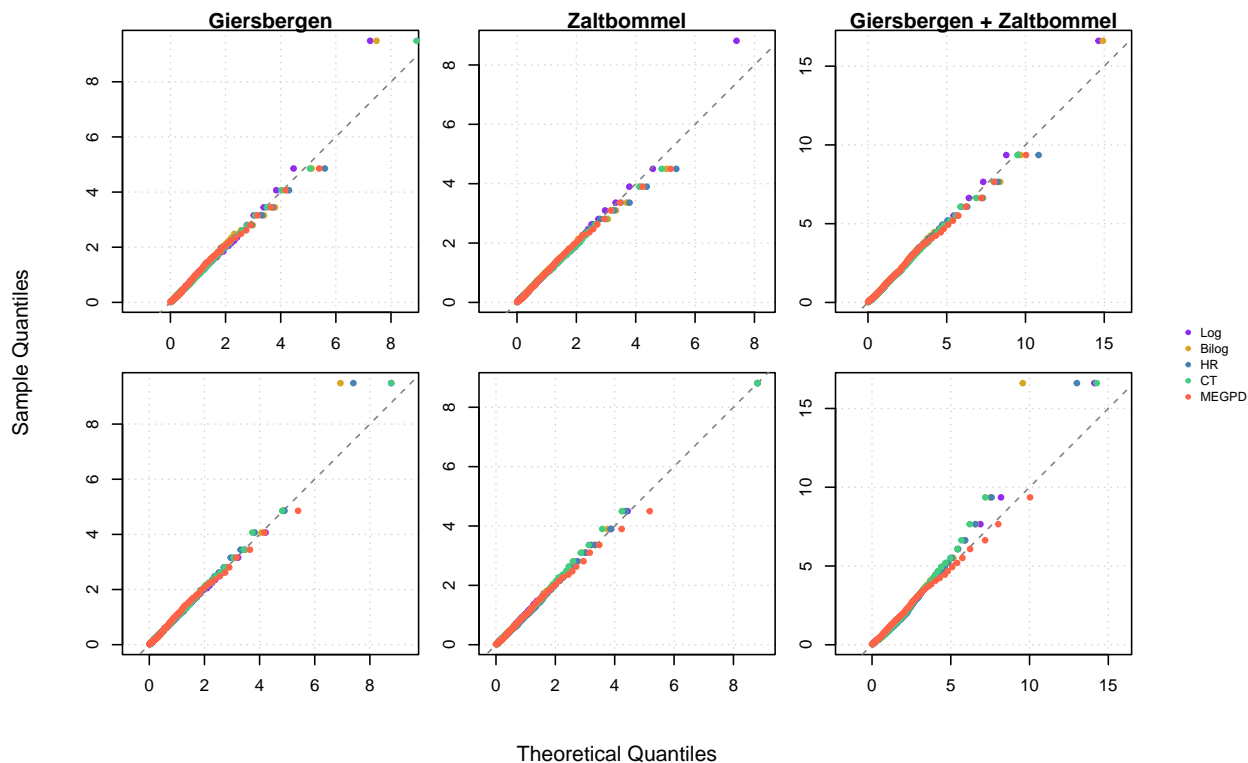


Figure A.10: QQ-plots for marginal (left and middle) and joint (right; summarized by the sum across stations) distributions, comparing classical bivariate GP models fitted to the upper (top) and lower (bottom) tails versus our multivariate eGPD fitted to the entire dataset, for the Giersbergen–Zaltbommel pair. Thresholds are selected as 2.80 mm (Giersbergen) and 2.81 mm (Zaltbommel) for the upper tail (after rescaling by the empirical standard deviation). For readability, the QQ-plots are displayed after transforming data from each tail to a common exponential scale. Classical bivariate GP fits include “Log”, “Bilog”, “HR”, and “CT”, together with “MEGPD”.